



Universiteit  
Leiden  
The Netherlands

## **Interaction of oxygen and carbon monoxide with Pt(111) at intermediate pressure and temperature : revisiting the fruit fly of surface science**

Bashlakov, D.

### **Citation**

Bashlakov, D. (2014, October 14). *Interaction of oxygen and carbon monoxide with Pt(111) at intermediate pressure and temperature : revisiting the fruit fly of surface science*. Retrieved from <https://hdl.handle.net/1887/29023>

Version: Corrected Publisher's Version

License: [Licence agreement concerning inclusion of doctoral thesis in the Institutional Repository of the University of Leiden](#)

Downloaded from: <https://hdl.handle.net/1887/29023>

**Note:** To cite this publication please use the final published version (if applicable).

Cover Page



Universiteit Leiden



The handle <http://hdl.handle.net/1887/29023> holds various files of this Leiden University dissertation

**Author:** Bashlakov, Dmytro

**Title:** Interaction of oxygen and carbon monoxide with Pt(111) at intermediate pressure and temperature : revisiting the fruit fly of surface science

**Issue Date:** 2014-10-14

*Interaction of Oxygen and Carbon Monoxide with  
Pt(111) at Intermediate Pressure and Temperature:  
Revisiting the Fruit Fly of Surface Science*

Proefschrift

ter verkrijging van  
de graad van Doctor aan de Universiteit Leiden,  
op gezag van de Rector Magnificus prof. mr. C.J.J.M. Stolker,  
volgens besluit van het College voor Promoties  
te verdedigen op dinsdag 14 oktober 2014  
klokke 11:15 uur

door

Dmytro Bashlakov

geboren te Ossora

in 1980

Promotiecommissie

Promotor: prof. dr. M.T.M. Koper

Co-promotors: dr. A.I. Yanson

dr. L.B.F. Juurlink

Overige leden: dr. I.M.N. Groot

prof. dr. B.E. Nieuwenhuys

prof. dr. J. Brouwer

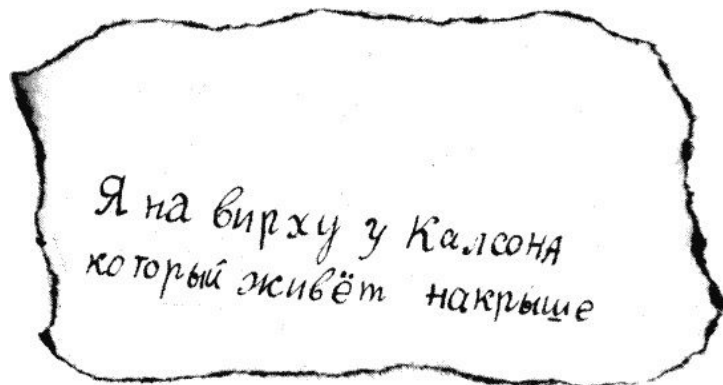
prof. dr. B. Dam (TU Delft)

prof. dr. P. Rudolf (Rijksuniversiteit Groningen)

## Contents

<b>Chapter 1 Introduction and literature overview</b> .....	5
1.1. Introduction.....	6
1.2. Catalysis.....	7
1.3. Surface science approach.....	9
1.3.1. Oxygen interaction with Pt(111).....	12
1.3.2. Carbon monoxide interaction with Pt(111).....	13
1.3.3. CO oxidation on Pt(111).....	14
<b>Chapter 2 Experimental instruments and techniques</b> .....	21
2.1. Omicron system.....	22
2.1.1. Vacuum system.....	22
2.1.2. Auger electron spectroscopy.....	23
2.1.3. Low energy electron diffraction.....	24
2.1.4. Scanning tunneling microscopy.....	26
2.1.5. Sample preparation.....	30
2.2. Lionfish.....	32
2.2.1. Vacuum system.....	32
2.2.2. Temperature programmed technique.....	32
2.2.3. Sample preparation.....	33
<b>Chapter 3 Subsurface oxygen on Pt(111)</b> .....	37
3.1. Introduction.....	38
3.2. Experimental section.....	39
3.3. Results and discussion.....	40
3.3.1. Oxygen adsorption at various temperatures.....	40
3.3.2. Surface structure.....	44
3.3.3. Oxygen reactivity towards CO oxidation.....	46
3.3.4. $^{16}\text{O}/^{18}\text{O}$ isotope exchange.....	48
3.4. Conclusions.....	49

<b>Chapter 4 Carbon monoxide oxidation on the Pt(111) surface at room temperature: STM and LEED studies.....</b>	<b>53</b>
4.1. Introduction.....	54
4.2. Experimental section.....	55
4.3. Results and discussion.....	58
4.3.1. STM and LEED.....	58
4.3.2. Mass spectrometry.....	65
4.3.3. Effect of CO poisoning on oxygen adsorption.....	67
4.4. Conclusions.....	69
<b>Chapter 5 Correlating surface activity and STM current transients during CO oxidation on Pt(111).....</b>	<b>73</b>
5.1. Introduction.....	74
5.2. Measurement approach and technique.....	75
5.3. Experiment and Results.....	77
5.4. Discussion.....	84
5.5. Summary.....	85
<b>Summary.....</b>	<b>89</b>
<b>Samenvatting.....</b>	<b>91</b>
<b>Curriculum Vitae.....</b>	<b>94</b>



---

## **Chapter 1**

### **Introduction and literature overview**

## 1.1. Introduction

Evolution and industrialization of human society is tightly connected to the use of metals. The first countries in the modern meaning of this word (distinct borders, defined policy and society organization) appear in the Bronze Age, when humans learned how to smelt and handle copper. Since then, metals began to be used not only for “primitive work” but also for specific “smart” applications. Besides being good construction materials due to their strength and plasticity, their unique electronic properties allow them to be used in functional devices. It is hard to imagine the functioning of the Large Hadron Collider without the niobium-titanium alloy used in the superconducting magnets or the development of modern computers without hard disc drives employing the giant magneto-resistance effect for information storage.

The application of metals as catalysts revolutionized the emerging chemical industry as well. Steam reforming is one of many examples of current industrial scale production of chemicals. Here, nickel is used for the production of hydrogen from fossil fuels and water. This reaction is the main source of hydrogen for ammonia production in the Haber-Bosch process [1]. In this nitrogen fixation reaction,  $\text{NH}_3$  is synthesized from nitrogen and hydrogen with the help of iron as a catalyst. As the initial component for artificial fertilizers, ammonia now “feeds” the continually growing population of the planet. A major advantage of using metals in industrial catalysis is that they are present as a solid during the reaction. It simplifies technological processes for the separation of products, which are typically present in the gas or liquid phase.

The demand for renewable energy sources as a basis for developing the post-industrial society delivers new challenges for commercial use of metals. Hydrogen is nowadays considered an alternative for fossil fuels. In the “Hydrogen Economy”, the target is an infrastructure where hydrogen is used as the energy carrier. Even though the process seems economically viable, at present steam reforming of methane can only be a temporary solution for the production of hydrogen as it consumes fossil fuels [2]. Electrolysis of water run on “green” electricity (wind, sunlight, hydropower, etc.) can be a permanent solution for this task.



Platinum is part of the puzzle for developing a closed materials cycle-renewable energy system. Its application in fuel cells already provides an alternative for combustion engines for transportation. In dye-sensitized solar cells platinum is used as a cathode. These cells are more attractive for household applications than semiconductor analogs due to the number of advantages such as smaller weight, lower production costs, and ability to work at low light intensity [3]. The real challenge for fundamental science now is to answer the question: “Why are some materials so unique?” Fully understanding the physics and chemistry may eliminate the need for expensive catalytic materials such as platinum by substitution with cheaper analogs providing similar performance.

This thesis uses the surface science approach to address questions regarding the interaction of oxygen with platinum and its subsequent reaction with carbon monoxide. A Pt(111) single crystal surface is used as a model for the catalyst. Chapter 1 provides an overview of the literature on the subject. The description of employed experimental techniques and their backgrounds are presented in Chapter 2. Chapter 3 discusses the adsorption of oxygen on Pt(111) at various temperatures and its role in the oxidation of carbon monoxide. Chapter 4 gives an atomic scale insight into the reaction between adsorbed oxygen and carbon monoxide for different ratios of oxygen and carbon monoxide pressures. In Chapter 5, the reaction between CO and oxygen on Pt(111) was used to register noise in tunneling current due to diffusion and recombination of molecules on the catalytically active surface, to draw conclusions on the most likely rate-limiting step in the process.

## 1.2. Catalysis

As stated previously, catalysis plays a major role in the industrial production of chemicals. The additional component needed to increase the reaction rate is called “catalyst”. A catalyst is involved temporarily in the chemical path of the reaction but does not appear as a final product. The principal scheme of a catalytic reaction can be described with the potential energy diagram (Figure 1.1) where the initial and the final states of the system are presented for the reactants **A** and **B** and the reaction product **P<sub>AB</sub>**, respectively. In a non-catalyzed reaction, the final state is reached by overcoming a potential energy barrier with activation energy **E<sub>a</sub>**. The particular task of the catalyst is to provide an alternative path for the

reaction with smaller activation energy  $E_a$ . In such case, a single reaction event proceeds via binding both or one of the reactants **A** and **B** to the catalyst first. Subsequently, reaction between reactants occurs with an activation energy smaller than for the non-catalyzed reaction. Finally, the formed product  $P_{AB}$  detaches from the catalyst so that the latter returns to its initial state and the next binding-reaction-detaching cycle can proceed.

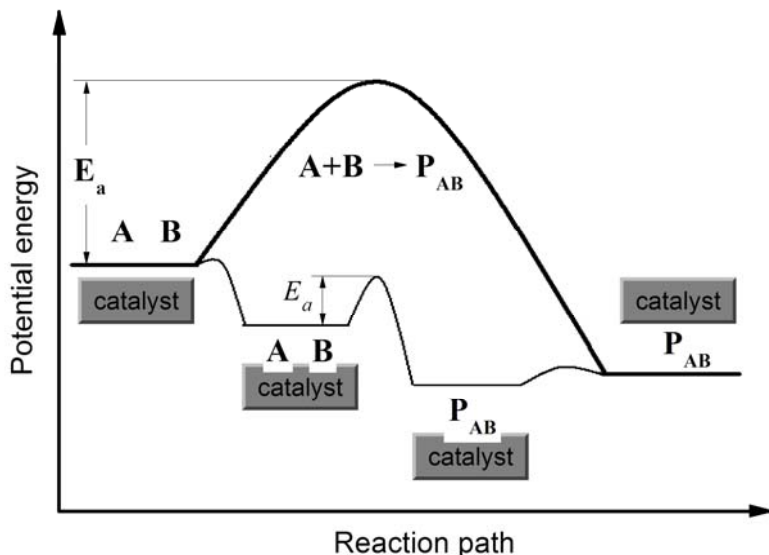


Figure 1.1. Potential energy diagram for a non-catalyzed and catalyzed reaction (reproduced from [4]).

There is a continuous search for better catalysts in order to optimize existing chemical processes as well as to introduce new ones. The performance of the catalyst is characterized by its activity, selectivity and stability. The meaning of these properties can also be explained by using the simple picture of the potential energy diagram:

- i. *Activity* of the catalyst describes how much product can be produced in the catalytic reaction over a period of time. The amount of product is determined by the activation energy  $E_a$  in such a way that the time needed for a single reaction reduces with the lowering of  $E_a$ . As a consequence, a catalyst with lower activation energy will convert more species **A** and **B** into  $P_{AB}$  over a certain period of time and will show higher activity (reaction rate) than a catalyst with higher activation energy under otherwise identical conditions.

- ii. If the desired product of reaction is the chemical  $P_{AB}$ , formation of different species ( $P_{BB}$ ,  $P_{AA}$ ,  $P_{ABA}$ , etc.) leads to an ineffective use of the feedstock. If the catalyst serves to reduce the activation energy only for the desired product ( $P_{AB}$ ) while the reaction path for other species remains unchanged or becomes more difficult, the catalyst *selectively* accelerates the reaction for useful product.
- iii. *Stability* indicates how long a catalyst can serve before losing its catalytic properties. Theoretically, the  $A + B \xrightarrow{\text{catalyst}} P_{AB}$  reaction cycle can be repeated indefinitely, however, the side products (like  $P_{BB}$ ,  $P_{AA}$ ,  $P_{ABA}$ , etc.) can also bind to the catalyst. If this chemical bond is strong, all active sites will be blocked after some time by the side products and the catalyst will lose its activity. A stable catalytic performance can also be influenced by the morphological changes of a catalyst.

The field of catalysis can be roughly divided in two parts. In homogeneous catalysis the reactant and catalyst are present in the same phase. In heterogeneous catalysis the catalyst and reactants are in different phases. To a large extent, industrial catalysis relies on heterogeneous catalysis where metal surfaces serve to bind reactants from the gaseous or liquid phase. A concept first introduced by Irving Langmuir [5] states that the surface serves as a two-dimensional lattice for molecular adsorption. The adsorbed molecules or atoms can diffuse across the surface approaching each other for reaction or desorb back into the gas/liquid. The rate of reaction strongly depends on the adsorption energy (i.e. the energy levels of adsorbed **A** and **B** in Figure 1.1) of the molecules to the surface and is described by the Sabatier principle [1]: The interaction of the adsorbants and the surface should be just right to obtain maximum reaction rate (activity). If the molecules are bound too weakly, they can leave the surface before reaction occurs. For very high adsorption energies, molecules will accumulate on the surface and block the active sites for adsorption of the new reactants, thus causing deactivation of the catalyst.

### 1.3. Surface science approach

Time dependent product analysis for an industrial catalyst is typically performed with techniques such as chromatography or mass spectrometry. This approach is useful in collecting information about the overall catalyst activity, selectivity and stability, while varying the macroscopic parameters

of reaction (temperature, pressure, reactants composition, etc.). The whole system, however, remains a “black box” for understanding fundamental steps of reaction. This is mostly due to the complex structure of the catalyst. Catalytically active nanoparticles are not uniform and are generally deposited onto an inactive support that often has little or no long-range structure. It is difficult to separate the contributions to the overall reaction rate from different crystal facets of the nanoparticles. The *surface science approach* studies catalytic reactions on well defined single crystal surfaces (Figure 1.2). In case of reactants present in the gas phase, the single crystal is cleaned and stored under UHV conditions ( $\sim 10^{-10}$  mbar) prior to its exposure to the reactants.

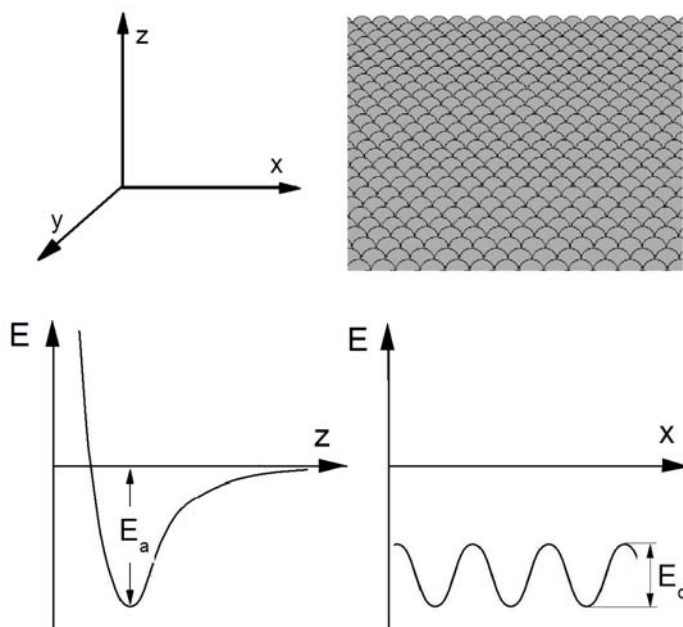


Figure 1.2. Potential energy diagram in direction perpendicular to the surface (bottom left) and along the surface (bottom right) for an adsorbate on a single crystal surface (top right), reproduced from [7].

The interaction between adsorbates and the surface can be illustrated with the potential energy diagram [6] shown on Figure 1.2. The minimum energy of the system is defined by the equilibrium state in which repulsive and attraction forces compensate each other. The repulsion force acts between the ionic cores of adsorbates and surface atoms. The attraction involves either van der Waals interactions (physisorption) or formation of a

chemical bond between molecules/atoms and surface (chemisorption). The position of the minimum in the energy diagram defines the distance of a molecule from the surface in the adsorbed state, while the decrease in the potential energy relative to the state for infinite distance  $z$  between adsorbate and the surface can be seen as the adsorption energy  $E_a$  of this molecule.

The binding energy of an adsorbate depends on its position on the surface [8]. The surface can be seen as a matrix of adsorption sites with largest adsorption energies (lowest potential energies) separated by a potential energy barrier ( $E_d$ ). To move across the surface, an adsorbate has to jump over this potential barrier. Figure 1.2 represents a potential energy surface for the diffusion of an adsorbate along the  $x$  direction. The average time  $\tau$  an adsorbate stays in one adsorption site can be estimated as [7]:

$$\tau \sim \exp\left(-\frac{E_d}{kT}\right),$$

so, that at low temperatures ( $kT \ll E_d$ ), an adsorbate will stay in the adsorption site almost indefinitely. For  $kT \geq E_d$  the residence time of adsorbate is limited and it can move across the surface if the nearest adsorption sites are not all occupied. If an adsorbed particle is surrounded by others, it will stay in the same adsorption site, unless it has energy higher than  $E_a$  to return into the gas phase (desorb) or react with a neighbor. When all adsorption sites are occupied, the surface has reached the saturation coverage  $\theta = n_a/n_s$ , where  $n_a$  and  $n_s$  are the maximum density of adsorbed particles and the density of atoms on the surface of the catalyst, respectively.

The previous description is valid if there is no possibility for recombinative desorption or other forms of reaction. Otherwise, when  $E_a > kT \geq E_d$  adsorbed molecules/atoms can approach and react with each other by forming a new molecule. The latter will leave the surface if the condition  $E_a^{\text{new molecule}} < kT$  is valid.

As mentioned above, the research subjects of this thesis are the adsorption of oxygen and the reaction between oxygen and carbon monoxide on the Pt(111) surface. Detailed knowledge about adsorption sites of O and CO and the mechanism of chemisorption is essential to understand the reaction path of O and CO reacting to  $\text{CO}_2$ . A brief summary of the state-of-the-art of these three topics is given in the next three sections.

### 1.3.1. Oxygen interaction with Pt(111)

The interaction of molecular oxygen with platinum can be illustrated with the energy diagram of Figure 1.3a [6, 9]. In the final state of adsorption  $O_2$  dissociates into two atoms by going through the intermediate state of chemisorbed  $O_2$ . Indirectly, this path was observed first in TPD experiments for a cold Pt(111) surface exposed to  $O_2$  [10, 11]. A subsequent linear increase of the sample temperature showed two desorption peaks for oxygen. The first desorption peak at 160 K was assigned to molecularly chemisorbed oxygen. A second broad peak with a maximum at  $\sim 750$  K was assigned to recombinative desorption of atomic oxygen. Using electron energy loss spectroscopy (EELS) it was confirmed that two different types of oxygen are present on Pt(111) at temperatures above 160 K [12-14]. Insight into the dissociation mechanism was delivered later by STM experiments. These showed that  $O_2$  adsorbs on bridge sites of platinum prior to dissociation and that oxygen atoms occupy three-fold hollow fcc sites after dissociation [15-17].

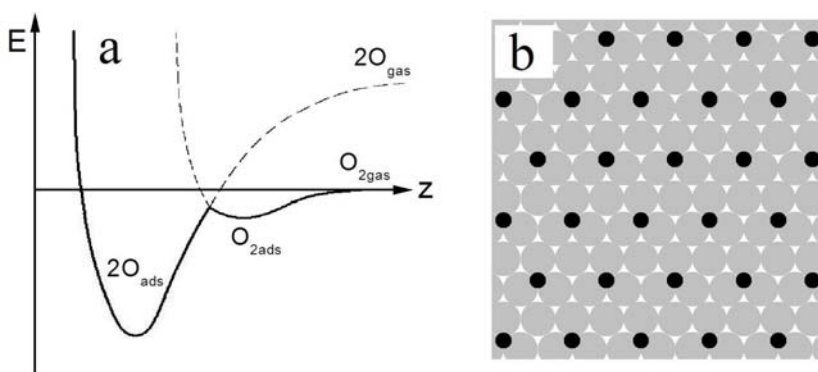


Figure 1.3. a) Energy diagram for dissociative adsorption of diatomic molecule ( $O_2$ ). b)  $O$ -p(2x2)-Pt(111) surface structure with 0.25 ML coverage for the layer of atomic oxygen (black circles) dissociatively adsorbed onto the (111) platinum crystal plane (grey circles).

Continuous exposure of a Pt(111) surface to molecular oxygen at room temperature leads to the formation of a layer of atomic oxygen ordered into a p(2x2) structure [18, 19] as shown on Figure 1.3b. This layer is characterized by (2x2) diffraction patterns in low energy electron diffraction (LEED) [9, 20]. It is interesting to note that (2x2) patterns become visible long before the oxygen layer reaches saturation [9]. This observation is in

agreement with STM measurements [15] showing that oxygen atoms prefer to organize into  $p(2 \times 2)$  islands indicating “an indirect attractive O-O interaction mediated through the electronic system of the substrate” [7].

Above room temperature, the mobility of platinum atoms starts to play a role in the interaction of platinum with oxygen [21, 22]. STM measurements showed significant restructuring (roughening) of Pt(110) and Pt(111) surfaces in an oxygen atmosphere of 1 bar at temperatures above 400 K [23, 24]. XRD studies reveal the formation of  $\alpha$ -PtO<sub>2</sub> on both crystallographic surfaces at identical conditions [25, 26]. This oxide structure on Pt(111) was found to be stable for O<sub>2</sub> pressures down to 1 mbar [26] indicating that not only temperature but also oxygen pressure is important for the oxide formation. Although most studies for the O<sub>2</sub>-Pt(111) system performed under high vacuum conditions did not focus on oxygen adsorption at temperatures above 300 K, some reported that at enhanced temperatures the amount of oxygen adsorbed on the Pt(111) surface is three to five times higher than expected from the O- $p(2 \times 2)$  layer [27-29]. Since platinum is a primary catalyst for oxidation reactions [1], an understanding of the alteration of catalytic properties of Pt(111) by high levels of surface oxidation is required [30, 31].

### 1.3.2. Carbon monoxide interaction with Pt(111)

Carbon monoxide chemisorbs on platinum as a diatomic molecule without dissociation [32] via formation of a chemical bond between carbon and platinum atoms [33]. The energy of this bond is rather low compared to the adsorption energy for atomic oxygen [34, 35]. Carbon monoxide desorbs from the Pt(111) surface at temperatures between 320-350 K, as derived from temperature programmed desorption (TPD) experiments [36-38]. EELS [38, 39] and infrared spectroscopy measurements [40, 41] reveal two types of adsorption sites: on-top of platinum atoms and on bridge sites between two platinum atoms. The difference between the CO adsorption energy for on-top and bridge sites is small [34, 42]. This causes high mobility of carbon monoxide on the platinum surface [34, 37]. The latter was noticed first in LEED experiments [32, 36]: the diffraction patterns from an unsaturated CO- $(\sqrt{3} \times \sqrt{3})R30^\circ$ -Pt(111) layer (Fig.1.4a) with 1/3 ML coverage became visible only after the sample was cooled sufficiently (150-170 K) [43]).

The saturation coverage of the CO-Pt(111) layer varies continuously with the CO pressure to which the surface is exposed [44]. A maximum

coverage of  $\sim 0.7$  ML can be reached, depending on the adsorption conditions [36]. At high vacuum conditions ( $10^{-8}$ - $10^{-7}$  mbar) and room temperature, the equilibrium saturation coverage is 0.5 ML. The CO layer is ordered into a commensurate  $c(4 \times 2)$  structure. This was initially concluded from LEED data [33] and later confirmed by scanning tunneling microscopy (STM) measurements [45]. In this structure, equal numbers of CO molecules adsorb on two high symmetry sites (on-top and bridge) as illustrated in Figure 1.4b. A coverage of CO molecules above 0.5 ML can be obtained under the high vacuum conditions by cooling the platinum surface below 170 K in a CO atmosphere [36, 38, 41] or by increasing the CO pressure above  $10^{-6}$  mbar at room temperature [46]. Such treatment leads to restructuring of the  $c(4 \times 2)$  layer into an incommensurate layer in which CO molecules are compressed closer to one other [47, 48] and the repulsive CO-CO interaction forces them to move from the high symmetry adsorption sites [47-49], as shown in Figure 1.4c.

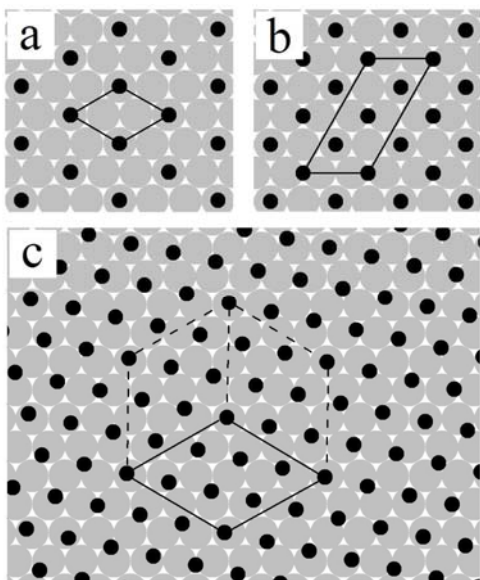


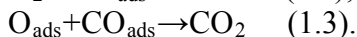
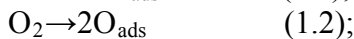
*Figure 1.4. Platinum surface (grey circles) with carbon monoxide (black circles) adsorbed into: a)  $(\sqrt{3} \times \sqrt{3})R30^\circ$  structure with  $1/3$  ML coverage; b)  $c(4 \times 2)$  structure with 0.5 ML coverage; c) incommensurate structure with CO coverage  $\approx 0.56$  ML.*

### 1.3.3. CO oxidation on Pt(111)

The reaction of CO oxidation on platinum follows the Langmuir-Hinshelwood mechanism [50, 51], which states that both reactants are



adsorbed on the surface when the reaction occurs. The reaction steps can be described with following three equations:



Reaction step (1.2) is sensitive to the presence of CO on the surface in the way that increasing the CO coverage inhibits oxygen dissociation [52]. On the other hand, the oxygen-covered Pt(111) surface is open for CO adsorption [53, 54]. Therefore, in coadsorption/titration experiments oxygen is the first component to be adsorbed on the surface [50, 53-58]. Gland and Kollin [55] were the first to demonstrate that reaction step (1.3) is thermally activated. The formation of CO<sub>2</sub> happens at temperatures above 250 K. The activation energy for this reaction step was found to be different for a high oxygen coverage ( $E_a \approx 0.5$  eV) compared to a low coverage of oxygen and CO ( $E_a \geq 1$  eV) [50, 54-58]. Using DFT calculations Alavi et al. [59] obtained a potential barrier of 1eV for the recombination reaction between CO and the oxygen atom adsorbed in the configuration (I) shown in Figure 1.5.

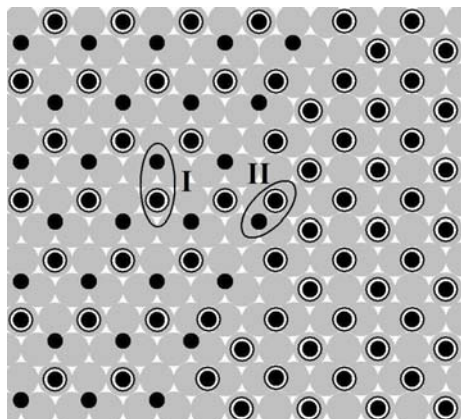


*Figure 1.5.  $p(2 \times 2)$  oxygen layer coadsorbed with CO (left part) in contact with  $c(4 \times 2)$  layer of CO (right part) The oxygen atoms and CO molecules are shown by small black circles and white and black circles, respectively.*

For a CO molecule placed at the bridge site closer to an oxygen atom (configuration II on Figure 1.5) the activation energy for reaction reduces to  $\approx 0.5$  eV. This suggests that in configuration (II) the activation time ( $\tau \sim \exp(E_a/kT)$ ) for reaction step (1.3) is shorter than in configuration (I). STM titration experiments [58] confirmed that at the border between CO-O  $p(2 \times 2)$  and CO-covered parts of the surface the reaction rate for O-CO recombination is higher than inside the CO-O  $p(2 \times 2)$  islands. The results presented in the Chapter 4 of this thesis support this observation.

This brief overview shows that the general mechanism for the CO oxidation is well understood: two species pre-adsorbed on specific adsorption sites come together and associate. However, several aspects require more attention to form a complete atomistic picture, such as how the formation of the platinum surface oxide at elevated temperature [30, 31] impacts on CO oxidation and how the CO poisoning [53-58] ceases the steady state oxidation reaction.

Chapter 3 deals with the first question. The experiment, which combines Temperature Programmed Reaction Spectroscopy (TPRS), Low Energy Electron Diffraction (LEED) and Scanning Tunneling Microscopy (STM) measurements, demonstrates that the Pt(111) surface can dissociatively adsorb more oxygen than 0.25 ML. This happens when the surface is exposed to oxygen at high vacuum conditions and elevated temperatures (400-600 K). Part of the oxygen migrates into the subsurface region. Interestingly, subsurface oxygen shows a much lower reactivity toward the oxidation of co-adsorbed CO, and moreover it does not influence the oxidation properties of the surface-bound oxygen.

In Chapter 4 oxidation of CO is studied at room temperature with STM and LEED for different ratios of oxygen and CO pressures in the gas phase. It will be shown there that the difference in the adsorption mechanisms of O<sub>2</sub> and CO, leads to a different dynamics of CO poisoning of the Pt(111) surface. For ratios close to the CO poisoning regime, the surface reaction causes the formation of a complex surface structure consisting of separated islands of ordered oxygen atoms and disordered regions containing carbon monoxide. With excess CO in the gas mixture, the surface becomes covered by a CO layer which blocks O<sub>2</sub> dissociation. With excess O<sub>2</sub>, the surface is covered by a p(2x2) oxygen layer, which remains active for CO→CO<sub>2</sub> conversion.

The attempt to measure the noise signature in the tunneling current during the surface reaction is described in Chapter 5. Based on the idea that recombination and diffusion of adsorbed species should cause changes in the local density of states on the surface, it was assumed that a higher noise level will be detected for the platinum surface brought in contact with gaseous mixture of CO and O<sub>2</sub> than for the platinum surface in vacuum. Indeed, an enhanced noise level compared to bare surface was observed experimentally for a Pt(111) surface in contact with O<sub>2</sub> and with a mixture of CO and O<sub>2</sub>, suggesting that the mobility of O on the surface is responsible for the enhanced noise levels and may therefore be a slow step in the overall reaction rate.

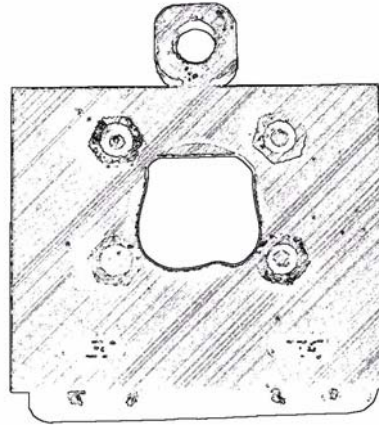
## References:

- [1] B. K. Hodnett, F. J. J. G. Janssen, J. W. Niemantsverdriet, V. Ponec, R. A. van Santen, and J. A. R. van Veen, *Catalysis: An Integrated Approach*, Elsevier Science, Amsterdam, 2000.
- [2] J. N. Armor, *Applied Catalysis A: General* 176 (1999) 159.
- [3] M. Gratzel, *Nature* 414 (2001) 338.
- [4] I. Chorkendorff and J. W. Niemantsverdriet, *Concept of modern catalysis and kinetics*, Wiley-VSH, Weinheim, 2003.
- [5] I. Langmuir, *Journal of the American Chemical Society* 40 (1918) 1361.
- [6] J. E. Lennard-Jones, *Transactions of the Faraday Society* 28 (1932) 333.
- [7] G. Ertl, *Reactions at solid surfaces*, Wiley, Berlin, 2009.
- [8] K. W. Kolasinski, *Surface Science: Foundation of Catalysis and Nanoscience*, Wiley, West Chester, 2008.
- [9] H. P. Bonzel and R. Ku, *Surface Science* 40 (1973) 85.
- [10] J. L. Gland, *Surface Science* 93 (1980) 487.
- [11] P. R. Norton, *Surface Science* 47 (1975) 98.
- [12] N. R. Avery, *Chemical Physics Letters* 96 (1983) 371.
- [13] P. Nolan, *The Journal of Chemical Physics* 111 (1999) 3696.
- [14] H. Steininger, S. Lehwald, and H. Ibach, *Surface Science* 123 (1982) 1.
- [15] B. C. Stipe, M. A. Rezaei, and W. Ho, *The Journal of Chemical Physics* 107 (1997) 6443.
- [16] J. Wintterlin, R. Schuster, and G. Ertl, *Physical Review Letters* 77 (1996) 123.
- [17] T. Zambelli, J. V. Barth, J. Wintterlin, and G. Ertl, *Nature* 390 (1997) 495.
- [18] K. Mortensen, C. Klink, F. Jensen, F. Besenbacher, and I. Stensgaard, *Surface Science* 220 (1989) L701.
- [19] P. R. Norton, J. A. Davies, and T. E. Jackman, *Surface Science* 122 (1982) L593.
- [20] J. Yoshinobu and M. Kawai, *The Journal of Chemical Physics* 103 (1995) 3220.
- [21] A. K. Galwey, P. Gray, J. F. Griffiths, and S. M. Hasko, *Nature* 313 (1985) 668.
- [22] C. Ellinger, A. Stierle, I. K. Robinson, A. Nefedov, and H. Dosch, *Journal of Physics-Condensed Matter* 20 (2008) 5.
- [23] B. L. M. Hendriksen and J. W. M. Frenken, *Physical Review Letters* 89 (2002) 046101.
- [24] S. C. Bobaru, Ph.D., Leiden University, The Netherlands, Leiden, 2006, p. 129.
- [25] M. D. Ackermann, T. M. Pedersen, B. L. M. Hendriksen, O. Robach, S. C. Bobaru, I. Popa, C. Quiros, H. Kim, B. Hammer, S. Ferrer, and J. W. M. Frenken, *Physical Review Letters* 95 (2005) 255505.

- [26] M. D. Ackermann, Ph.D., Leiden University, The Netherland, Leiden, 2007, p. 192.
- [27] D. Neuhaus, F. Joo, and B. Feuerbacher, *Physical Review Letters* 58 (1987) 694.
- [28] G. N. Derry and P. N. Ross, *Surface Science* 140 (1984) 165.
- [29] G. N. Derry and P. N. Ross, *Journal of Chemical Physics* 82 (1985) 2772.
- [30] W. X. Li and B. Hammer, *Chemical Physics Letters* 409 (2005) 1.
- [31] F. Gao, S. M. McClure, Y. Cai, K. K. Gath, Y. Wang, M. S. Chen, Q. L. Guo, and D. W. Goodman, *Surface Science* 603 (2009) 65.
- [32] H. Hopster and H. Ibach, *Surface Science* 77 (1978) 109.
- [33] D. F. Ogletree, M. A. Van Hove, and G. A. Somorjai, *Surface Science* 173 (1986) 351.
- [34] M. Lynch and P. Hu, *Surface Science* 458 (2000) 1.
- [35] Y. Y. Yeo, L. Vattuone, and D. A. King, *The Journal of Chemical Physics* 106 (1997) 392.
- [36] G. Ertl, M. Neumann, and K. M. Streit, *Surface Science* 64 (1977) 393.
- [37] C. T. Campbell, G. Ertl, H. Kuipers, and J. Segner, *Surface Science* 107 (1981) 207.
- [38] H. Steininger, S. Lehwald, and H. Ibach, *Surface Science* 123 (1982) 264.
- [39] H. Froitzheim, H. Hopster, H. Ibach, and S. Lehwald, *Applied Physics A: Materials Science & Processing* 13 (1977) 147.
- [40] H. Krebs and H. Lüth, *Applied Physics A: Materials Science & Processing* 14 (1977) 337.
- [41] B. N. J. Persson, M. Tushaus, and A. M. Bradshaw, *The Journal of Chemical Physics* 92 (1990) 5034.
- [42] E. Schweizer, B. N. J. Persson, M. Tüshaus, D. Hoge, and A. M. Bradshaw, *Surface Science* 213 (1989) 49.
- [43] J. S. McEwen, S. H. Payne, H. J. Kreuzer, M. Kinne, R. Denecke, and H. P. Steinruck, *Surface Science* 545 (2003) 47.
- [44] R. T. Vang, E. Laegsgaard, and F. Besenbacher, *Physical Chemistry Chemical Physics* 9 (2007) 3460.
- [45] M. O. Pedersen, M.-L. Bocquet, P. Sautet, E. Legsgaard, I. Stensgaard, and F. Besenbacher, *Chemical Physics Letters* 299 (1999) 403.
- [46] S. R. Longwitz, J. Schnadt, E. K. Vestergaard, R. T. Vang, I. Stensgaard, H. Brune, and F. Besenbacher, *The Journal of Physical Chemistry B* 108 (2004) 14497.
- [47] E. Kruse Vestergaard, P. Thostrup, T. An, E. Lægsgaard, I. Stensgaard, B. Hammer, and F. Besenbacher, *Physical Review Letters* 88 (2002) 259601.
- [48] M. Montano, K. Bratlie, M. Salmeron, and G. A. Somorjai, *Journal of the American Chemical Society* 128 (2006) 13229.
- [49] M. Tüshaus, W. Berndt, H. Conrad, A. M. Bradshaw, and B. Persson, *Applied Physics A: Materials Science & Processing* 51 (1990) 91.

- [50] C. T. Campbell, G. Ertl, H. Kuipers, and J. Segner, *The Journal of Chemical Physics* 73 (1980) 5862.
- [51] G. Ertl, *Surface Science* 299–300 (1994) 742.
- [52] M. Ehsasi, M. Matloch, O. Frank, J. H. Block, K. Christmann, F. S. Rys, and W. Hirschwald, *The Journal of Chemical Physics* 91 (1989) 4949.
- [53] J. L. Gland and E. B. Kollin, *Surface Science* 151 (1985) 260.
- [54] M. Kinne, T. Fuhrmann, J. F. Zhu, C. M. Whelan, R. Denecke, and H. P. Steinruck, *The Journal of Chemical Physics* 120 (2004) 7113.
- [55] J. L. Gland and E. B. Kollin, *The Journal of Chemical Physics* 78 (1983) 963.
- [56] I. Nakai, H. Kondoh, K. Amemiya, M. Nagasaka, T. Shimada, R. Yokota, A. Nambu, and T. Ohta, *The Journal of Chemical Physics* 122 (2005) 134709.
- [57] F. Zaera, J. Liu, and M. Xu, *The Journal of Chemical Physics* 106 (1997) 4204.
- [58] J. Wintterlin, S. Volkening, T. V. W. Janssens, T. Zambelli, and G. Ertl, *Science* 278 (1997) 1931.
- [59] A. Alavi, P. Hu, T. Deutsch, P. L. Silvestrelli, and J. r. Hutter, *Physical Review Letters* 80 (1998) 3650.





---

## Chapter 2

### Experimental instruments and techniques

In surface science, experiments are conducted in a well-controlled environment. Ultra high vacuum (UHV) conditions are often used for sample preparation and characterization. Results presented in this thesis were collected using two UHV instruments: The “Omicron” system (Chapters 3, 4 and 5) and the “Lionfish” system (Chapter 3). Both systems contain equipment for cleaning of single crystal surfaces and for characterization with surface sensitive techniques. These techniques are described in this chapter. High purity  $^{16}\text{O}_2$  (Messer 5.0), Ar (Messer 5.0), CO (Air Liquide 4.7), and  $^{18}\text{O}_2$  (Cambridge Isotope Laboratories, 97% isotope purity and  $\geq 99.9$  chemical purity) were used for sample cleaning and gas dosing.

## 2.1 The Omicron system

The Omicron system’s principal surface sensitive technique is Scanning Tunneling Microscopy (STM). Auger Electron Spectroscopy (AES) and LEED are supporting techniques used for surface characterization. The system consists of two UHV chambers, one load lock and a set of manipulators for sample/tip transfer. A custom made gas mixing manifold is connected by separate dosing lines to each of the UHV chambers. The pressure in the gas lines can be reduced to below  $10^{-3}$  mbar prior to filling them with gases.

### 2.1.1 Vacuum system

The preparation and analysis chambers both have a base pressure of  $\approx 2 \times 10^{-10}$  mbar as monitored with Bayard-Alpert type manometers. A gate valve separates the chambers. Both chambers can be evacuated using a combination of an ionization pump (Varian, Star Cell) and a turbo molecular pump (Pfeiffer, TMU-260). Gate valves allow for pumping on each chamber by either pump. The turbo molecular pump is switched off prior to STM measurements to reduce vibrations in the system. Similarly,



ionization pumps were switched off during sample cleaning and experiments involving oxygen doses.

The preparation chamber is equipped with leak valves and an ion gun for sample cleaning. This includes sputtering with argon ions and subsequent annealing of the sample. Single crystals are mounted in a sample holder with a built-in tungsten filament that faces the back side of the sample. The filament has electrical contacts which are isolated from the rest of the sample holder. It allows for radiative heating and electron bombardment heating from room temperature up to 1200 K. To this purpose, the preparation chamber has a manipulator with electrical connections to the sample holder's filament and thermocouple.

The analysis chamber is equipped with an Omicron variable temperature (VT) STM, a rear view LEED apparatus (VG RVL-900), an electron gun (VG LEG 63), a hemispherical electron analyzer for Auger spectroscopy (VG 100 AX), and a storage unit for six sample/tip holders. Two leak valves connected to the O<sub>2</sub> and CO gas lines allow for separate dosing of these gases in the analysis chamber. In addition, an initially prepared O<sub>2</sub>:CO gas mixture with required composition can be dosed by expansion from the small volume separated from the analysis chamber using a valve. An x,y,z-manipulator with 360° rotation is used for proper positioning of the sample for LEED and AES measurements.

### 2.1.2 Auger electron spectroscopy

AES is a surface sensitive technique used to characterize chemical composition of a sample's (near) surface. The mechanism of Auger electron emission is as follows. When surface atoms are bombarded by high energy electrons or photons, they can eject an electron from a core level of an atom and create a hole. This hole is filled by an electron from a higher energy level. The released energy may be transferred to a third electron, if this one is ejected into vacuum, it is called an Auger electron. The energy of Auger electrons depends only on the nature of the atom that emits them. Therefore, elemental analysis can be performed by measuring the energy spectrum of Auger electrons and comparing it to handbook spectra [1, 2].

In our system, a beam of electrons with 3 keV kinetic energy is used to produce Auger electrons. Energy spectra are recorded with a hemispherical electron energy analyzer. Carbon was found as the main contamination for samples introduced into the system. Sensitivity of the Auger spectrometer was tested for carbon and oxygen on the clean Pt(111) surface covered with

0.5 ML of CO. The lower sensitivity range was not determined due to the poor control over the dosing for smaller coverage. That is why a final evaluation of the surface quality was done with STM.

### 2.1.3 Low energy electron diffraction

In contrast to Auger spectroscopy, LEED technique is based on the elastic scattering of electrons. These electrons have a de Broglie wavelength  $\lambda$  defined by

$$\lambda = \frac{h}{\sqrt{2mE}}, \quad (2.1)$$

where  $h$  is Planck's constant,  $m$  is the mass of an electron and  $E$  is the electron energy. To calculate the wavelength in nanometers, equation (2.1) is also used in the form

$$\lambda(nm) = \sqrt{\frac{1.5}{E(eV)}}. \quad (2.2)$$

Therefore, for electrons with energies between 50 and 200 eV, which is typical in diffraction experiments,  $\lambda=0.2-0.1$  nm. This is comparable to interatomic distances. In LEED, the primary beam of electrons with fixed energy impinges onto a single crystal surface. Back-scattered electrons pass through electrostatic grids that select only the elastically scattered electrons. These are visualized on a hemispherical phosphorous screen. Constructive interference between the electrons results in a diffraction pattern on the screen. The pattern represents an image of the reciprocal lattice of the real surface. In reciprocal space, diffraction from a periodic structure follows the Laue condition, which is expressed in the following form for a two dimensional lattice [3]:

$$\vec{k}_{\parallel} - \vec{k}'_{\parallel} = m\vec{a}^* + l\vec{b}^*, \quad (2.3)$$

Here,  $\vec{a}^*$  and  $\vec{b}^*$  are the basis vectors of the surface in reciprocal space,

$m$  and  $l$  are integers,  $\vec{k}_{\parallel}$  and  $\vec{k}'_{\parallel}$  are the components of a wave vector

parallel to the surface for incident and scattered electrons, respectively. In the case of elastic scattering:

$$|\vec{k}| = |\vec{k}'| = \frac{2\pi}{\lambda}, \quad (2.4)$$

The basis vectors of the reciprocal lattice expressed via the real space basis vectors  $\vec{a}$ ,  $\vec{b}$  and the unit vector normal to the surface  $\vec{n}$ :

$$\vec{a}^* = \frac{2\pi\vec{b}\vec{n}}{\vec{a}(\vec{b} \times \vec{n})} \quad \text{and} \quad \vec{b}^* = \frac{2\pi\vec{a}\vec{n}}{\vec{a}(\vec{b} \times \vec{n})}, \quad (2.5)$$

or:

$$a^* = |\vec{a}^*| = \frac{2\pi}{a \sin(\angle \vec{a}\vec{b})} \quad \text{and} \quad b^* = |\vec{b}^*| = \frac{2\pi}{b \sin(\angle \vec{a}\vec{b})}. \quad (2.6)$$

The  $\sin(\angle \vec{a}\vec{b}) = S$  reflects the symmetry of the surface lattice, which can be rectangular ( $S=1$ ) or hexagonal ( $S=\sqrt{3}/2$ ). In case of an incident electron beam normal to the surface for the (10) diffraction spot ( $m=1, l=0$ ) the combination of equations (2.3), (2.4) and (2.6) gives:

$$\frac{2\pi}{\lambda} \sin(\theta) = \frac{2\pi}{aS}, \quad \text{or} \quad aS \sin(\theta) = \lambda \quad (2.7)$$

Therefore, the unit cell of an unknown surface lattice can be calculated from the LEED image, since the electron wave length ( $\lambda$ ) is given by equation 2.2,  $S$  can be assumed from the symmetry of the LEED image, and  $\sin(\theta)$  for the diffraction spots is defined from the dimensions of LEED optics. In case the sample is placed in the geometrical center of the hemispherical LEED screen (Figure 2.1a):

$$\sin(\theta) = \frac{C}{R}; \quad (2.8)$$

where  $R$  is the radius of curvature of the LEED screen and  $C$  is the distance from the center of LEED image to the diffraction spot. This equation cannot be applied if the sample is displaced from the geometrical center of the LEED optics as illustrated in Figure 2.1c. In Chapter 4 the period for the CO adlayer on the Pt(111) surface is calculated. The platinum diffraction pattern is used to calculate the displacement of the sample  $D=L-X$  (Figure 2.1b). By using the distance between platinum atoms ( $a=2.77 \text{ \AA}$ ), equation (2.7),

$$\varphi = \arcsin\left(\frac{2\lambda}{\sqrt{3}a}\right), \quad (2.9)$$

and trigonometric equations

$$\text{tg}(\varphi) = \frac{A}{L} \quad (2.10)$$

and

$$X = \sqrt{R^2 - A^2}, \quad (2.11)$$

the displacement D can be calculated from:

$$D = \frac{A}{\operatorname{tg}\left(\arcsin\left(\frac{2\lambda}{\sqrt{3}a}\right)\right)} - \sqrt{R^2 - A^2} \quad (2.12)$$

The angle  $\theta$  for the diffraction maximum of an unknown structure  $C'$  (Figure 2.1c) can be calculated from

$$\theta = \operatorname{arctg}\left(\frac{C'}{D + \sqrt{R^2 - C'^2}}\right). \quad (2.13)$$

In Chapter 4, the described expression (2.13) of a reflection angle  $\theta$  placed into equation (2.7) is used to determine the period of a Moiré pattern for the CO adlayer.

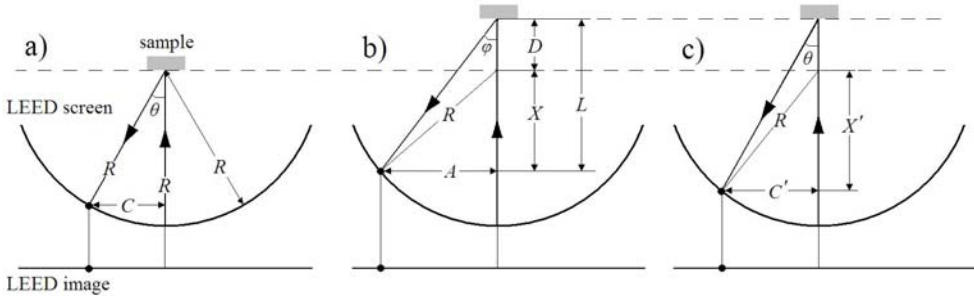


Figure 2.1 Schematic representation of a LEED experiment for a sample placed in the center of the LEED optics (a), or displaced by the distance D from it (b, c). The large arrows mark the incoming and the back-scattered beams of electrons.

#### 2.1.4 Scanning tunneling microscopy

The interpretation of LEED images is not always straightforward. Adsorbed molecules can arrange in domains with different orientations relative to the substrate and each of these will contribute to the LEED pattern. The power of scanning tunneling microscopy (STM) is that the

surface structure can be visualized locally with atomic resolution, thus any ambiguity about the adsorbate's arrangement can be ruled out [4]. The STM technique employs the effect of tunneling of electrons through the potential barrier created between an atomically sharp metal tip and a conductive surface. The tunneling current  $I_t$  can be detected when the tip approaches the surface and some voltage  $V_t$  is applied between them. The conductivity  $G$  of the tunnel barrier is [5]:

$$G = \frac{I_t}{V_t} \approx \exp(-2\kappa z) \cdot \rho(r_t, E_F), \quad (2.14)$$

where  $z$  is the tip-to-sample distance,  $\kappa$  is the decay constant for the electron wave function in vacuum and  $\rho$  is the local density of states of the surface at the Fermi level ( $E_F$ ) in the position of the tip  $r_t$ . Spatial changes in the local electron density of states follow the arrangement of the surface atoms. By moving the tip across the surface in  $x,y$  direction while adjusting the tip position to keep the tunnel current constant (constant current mode) and recording the  $z$  position of the tip, the topography of the surface can be measured with atomic resolution.

The sensitivity of the STM technique is governed by decay constant  $\kappa$ :

$$\kappa = \frac{\sqrt{2m\Phi}}{h} \approx 1 \text{ nm}^{-1}, \quad (2.15)$$

where  $h$  is Planck's constant,  $m$  is the mass of an electron and  $\Phi$  is the height of the potential barrier, which is equivalent to the work function of materials used in the STM experiment [6]. Using this value for the decay constant in equation (2.14), the tunnel current ratio at the same  $x,y$  tip position for different tip-to-surface distances is

$$\frac{I_t^I}{I_t^{II}} = \exp(-2\kappa(z^I - z^{II})), \quad (2.16)$$

The corrugation of the local density of states on metal surfaces is in the range of 5 to 20 pm [6]. Thus, changes in tunnel current of 10-50% should be detectable to measure the surface topography with atomic resolution. In other words, the contribution into the tunnel current from parasitic signals should be less than 10% for "flat" surfaces not to override the current variations caused by the surface topography. The origins of parasitic signals are typically mechanical vibrations and electronic crosstalk. To improve the resolution of any STM system, both components should be reduced to a minimum. Passive damping of external vibrations in the Omicron system

was realized by mounting the UHV set-up on a special floor that is decoupled from the rest of the building. Additional damping of vibrations was realized with an Eddy current damping stage on the STM scanner. It is hanging on springs inside the UHV chamber. Electronic crosstalk from external sources was effectively screened by the UHV chamber serving as a Faraday cage. In addition, grounding of electronic equipment to a common ground point prevents parasitic crosstalk into the tunnel current measurement circuit from the rest of the system.

Beside external factors that influence resolution, a highly important factor is the interaction of the tip with the surface. It has been observed experimentally that the ability to resolve every single atom on the surface depends on the tip state and geometry [6]. Preparation of an atomically sharp tip is an intricate part of the STM experiment itself. The results presented in Chapters 3, 4 and 5 were obtained with self-prepared tungsten tips. These tips were electrochemically etched in the loop-meniscus configuration (Figure 2.2a) from a 0.25 mm tungsten wire in a 2M solution of NaOH and with a platinum counter electrode. The bottom part of the wire was caught and used as a tip. The shape of the prepared tips was characterized in a scanning electron microscope (FEI Nova SEM). An etching routine of applying a DC voltage  $\geq 3\text{V}$  gave the most reproducible results: a single tip apex of 10-50 nm radius and a smooth finish of the tungsten surface (Figure 2.2b). At the same time, etching with a DC voltage  $< 2\text{V}$  or with an AC voltage often led to the formation of a rough tungsten surface, probably due to the uneven etching speed along different crystal planes. As a result, multiple apex tips were regularly produced, as shown in Figure 2.2c. The sharpest tips were selected and mounted into the tip holder shown in the inset of Figure 2.2d.

The tungsten oxide formed during etching has to be removed prior to using tips for scanning [7]. The tip apex was heated in an UHV environment by an emission current up to 200  $\mu\text{A}$ . This treatment yields a stable electron emission current in the 0-20 nA range, as shown in Figure 2.2d and a stable tunnel current under tunneling conditions.

Subsequent conditioning of the tips included scanning of an Au(100) single crystal surface. The advantage of using a gold sample is twofold:

- the gold surface stays almost indefinitely clean under UHV conditions;
- it is much easier to resolve the structure of the quasi-hexagonal reconstruction of the Au(100) surface ( $z$  corrugation  $\approx 0.5\text{\AA}$ ) than the atomic fine structure (corrugation  $\approx 0.1\text{\AA}$ ) [8].

All tips that showed stable emission current were able to resolve the reconstruction on the gold surface. To improve the spatial resolution further, pulses of a voltage of 2-3 V were applied over the tunnel junction. This treatment leads to restructuring of atoms on the tip apex and to improvement of the tip resolution. Tip conditioning was performed daily until the fine structure of the Au(100) surface was observed (Figure 2.3c).

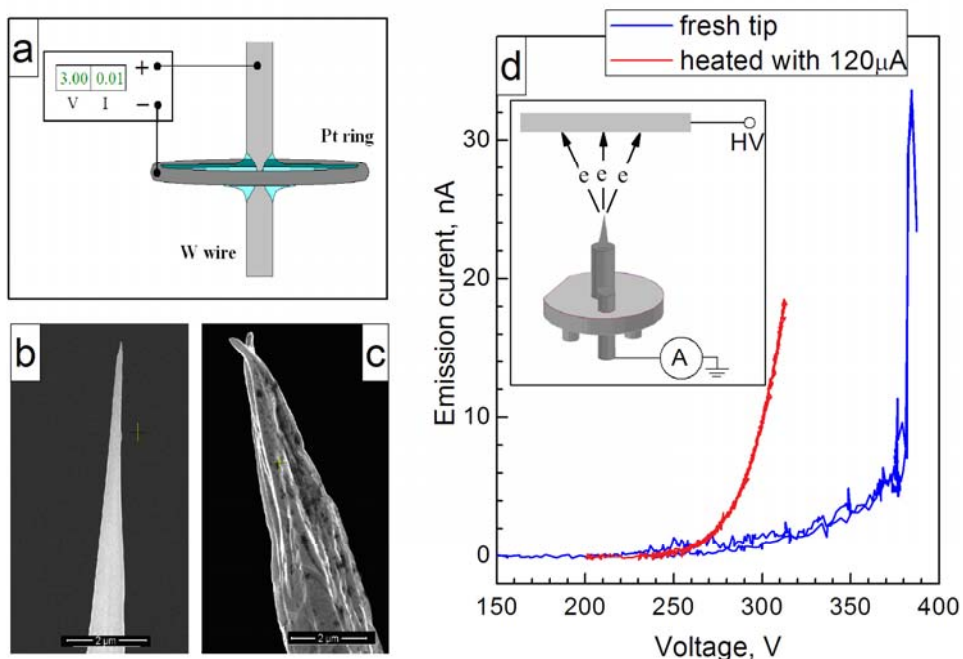


Figure 2.2 Stages of STM tip preparation for the Omicron system. Electrochemical etching in 2M NaOH solution (a). Validation of the tip geometry with SEM (b, c). (d) Tip conditioning inside the UHV chamber by an emission current induced through applying a high voltage between the tip and a counter electrode as shown in the inset. The  $I(V)$  emission curve in the 0-20 nA range for a fresh tip (blue line), and for the same tip after being heated with 120  $\mu$ A of emission current (red line).

## 2.1.5 Sample preparation

### *Au(100)*

A 1 mm thick flat gold single crystal with a  $5 \times 7 \text{ mm}^2$  elliptical shape exposing a polished (100) plane [9] was cleaned in the UHV system by several cycles of

- argon sputtering for 10 min at 600eV ion energy and 5-8  $\mu\text{A}$  ion current;
- annealing in vacuum at 700-720 K for 5 min.

This procedure removes the initial contamination (carbon and sulfur, Figure 2.3a) and gives an STM-grade clean surface as shown in Figures 2.3 b and c.

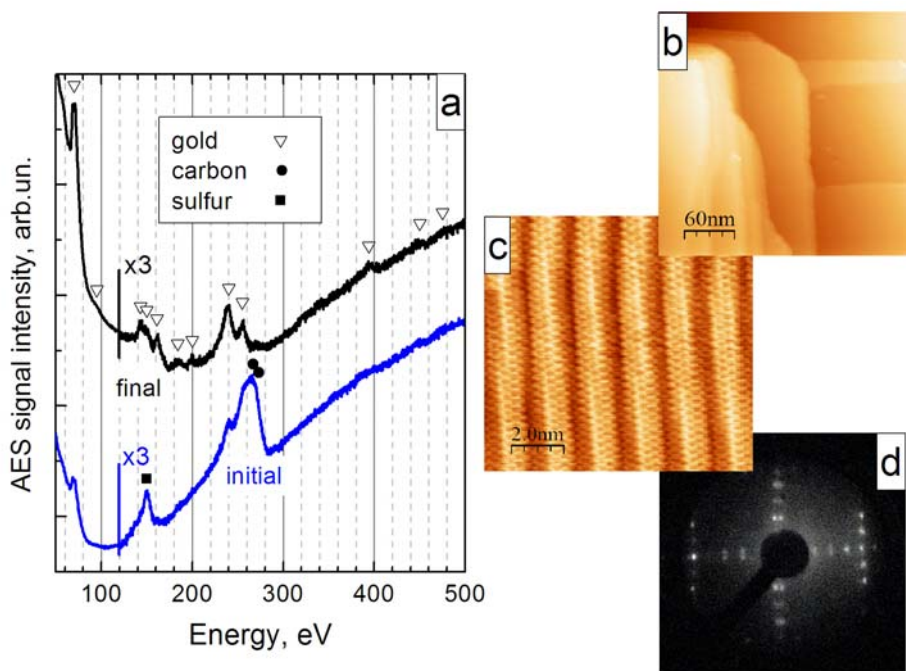


Figure 2.3 Validation of the quality of the *Au(100)* surface. Auger spectrum of the surface composition before (blue line) and after (black line) sputtering-annealing cycles (a). STM image of the  $260 \times 260 \text{ nm}^2$  surface area (b) and  $8.6 \times 8.6 \text{ nm}^2$  (c) for a clean surface. Fine structure of the quasi-hexagonal reconstruction observed with LEED at 60eV primary electron beam energy (d).



### *Pt(111)*

STM data presented in Chapters 3-5 were collected using a 1 mm thick 6 mm diameter circular single crystal mechanically polished along a (111) plane [9]. The sample was cleaned with several cycles of

- argon sputtering for 10 min at 800-1000 eV ion energy and 8-12  $\mu\text{A}$  ion current;
- heating for 10-30 min in  $3\text{-}6 \times 10^{-7}$  mbar of oxygen at 800-900 K to remove carbon, or annealing to 1100-1200 K in vacuum for 5 min.

The quality of the cleaning procedure was first verified by Auger spectroscopy (Figure 2.4a). After contamination levels dropped below the detection level of AES, the quality of the surface was monitored with STM. Sputtering-annealing cycles were repeated until an atomically-resolved, STM-clean surface was observed (Figure 2.4c). The daily cleaning routine included annealing in oxygen for half an hour and flashing to 1200 K in vacuum.

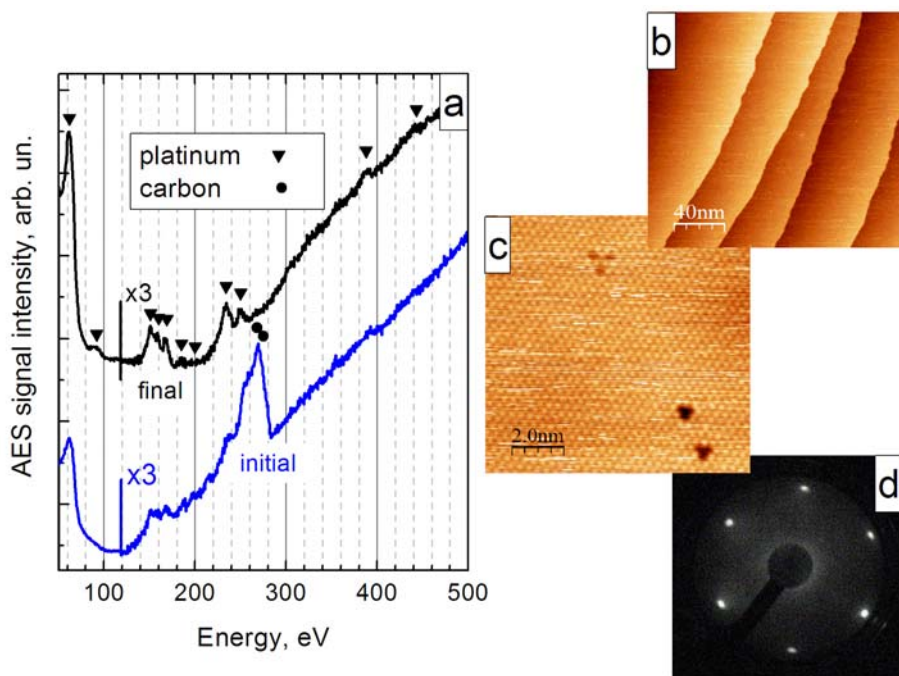


*Figure 2.4 Validation of the quality of the Pt(111) surface. Auger spectrum for the surface composition before (blue line) and after (black line) the sputtering-annealing cycles (a). STM topography of the 170x170nm surface area (b) and 8.6x8.6nm (c) for a clean surface. LEED image of the STM grade clean Pt(111) surface taken at the 68 eV beam energy (d).*

## 2.2. Lionfish

### 2.2.1 Vacuum system

The results of the TPD and temperature programmed reaction spectroscopy (TPRS) measurements, described in Chapter 3, were obtained using a home-build instrument named “Lionfish”. The system has a base pressure  $<2 \times 10^{-10}$  mbar which is achieved using two turbo molecular pumps placed in series (Pfeiffer TMU 521 and TMH 071) and a rotary vane pump (Pfeiffer Duo 10). The system hosted a 10 mm diameter and 1 mm thick platinum single crystal with one side polished to  $<0.1^\circ$  precision of (111) plane [9]. The sample was mounted on the differentially pumped manipulator with cooling by liquid nitrogen. The sample temperature was measured by a K-type thermocouple spot-welded to the side of the crystal. The filament was placed on the back side of the crystal. Radiative heating and electron bombardment were used for the sample heating with a PID controller (Eurotherm 2416). In combination with  $\text{LN}_2$ , cooling this yielded accurate control of sample temperature between 85 and 1300 K. The system is equipped with a quadrupole mass spectrometer (Balzers Prisma 200), a rear view LEED (LK Technologies RVL2000/8/R), a sputtering gun and leak valves for background dosing.

### 2.2.2 Temperature programmed techniques

TPD and TPRS belong to a class of techniques in which a reaction is monitored while the temperature of a sample changes [10]. These techniques allow to evaluate the surface coverage and activation energy for desorption/recombination of surface-bound species. During an experiment, the surface is first covered with adsorbates. Then the temperature of the sample is linearly increased while the reaction products are monitored with a mass spectrometer. The concept of temperature programmed measurements is related to the Arrhenius equation for the reaction rate,  $r$

$$r = A \exp\left(\frac{E}{kT}\right), \quad (2.17)$$

The desorption processes is described by the Polanyi-Wigner equation [11]:

$$r(t) = -\frac{d\theta}{dt} = \nu \theta^n(t) \exp\left(\frac{E}{RT}\right), \quad \text{where } T = T_0 + \beta t, \quad (2.18)$$

where  $r$  is the rate of desorption,  $t$  is time,  $\nu$  is the pre-exponential factor,  $\theta$  is the adsorbate coverage,  $n$  is order of desorption process,  $t$  is the time,  $E$  is activation energy of desorption,  $R$  is the gas constant, and  $T$  is the sample temperature which increases with the heating rate  $\beta$ . The number of molecules leaving the surface is detected as a change of the partial pressure

$P$  relative to the steady state background partial pressure in the vacuum system for the molecule of interest

$$\Delta P(t) \sim r(t).$$

As can be seen from (2.18), the pressure will increase first since the probability for the molecules to leave the surface increases while the temperature rises. At some point, the decrease in the surface coverage ceases to allow further pressure rise.  $\Delta P$  goes through a maximum and drops to zero when all adsorbed species have left the surface. The position of the maximum and the shape of the TPD spectra contain information about the activation energy and the order of the desorption process [12]. The area under the TPD spectrum is proportional to the surface coverage:

$$\theta = \int_0^{t_{\max}} \frac{d\theta}{dt} dt \sim \int_0^{t_{\max}} \Delta P(t) dt = \int_{T_0}^{T_{\max}} \Delta P dT. \quad (2.19)$$

Hence, with the proper system calibration, the surface coverage of the adsorbed species can be determined from the measured spectrum. In Chapter 3, various coverages of atomic oxygen were determined from the area of TPD spectra by comparing them to the TPD peak area of the O-p(2x2)Pt(111) layer with 0.25 ML coverage.

### 2.2.3 Sample preparation

The (111) surface of this Pt single crystal was cleaned with repeated cycles of Ar sputtering (600eV, 0.2-0.3  $\mu$ A) for 15 min, annealing in oxygen atmosphere ( $1-3 \times 10^{-7}$  mbar) at 900-1000 K for 5 min and annealing in vacuum at 1200 K for 5 min. LEED from the clean surface revealed a hexagonal diffraction pattern similar to what had been observed for a clean Pt(111) surface in the Omicron system (Figure 2.5).

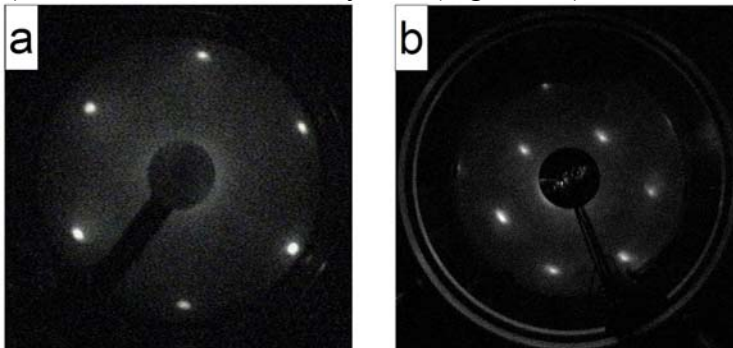


Figure 2.5 LEED images of two platinum single crystals with (111) plane from Omicron (a) and Lionfish (b) systems taken with 68 eV and 100 eV beam energy, respectively.

No additional structure was detected, although the diffraction spots show some elongation. This is ascribed to imperfect focusing of the electron beam.

The chemical quality of the surface was checked by tracing the TPD signals of CO, CO<sub>2</sub> and water after the surface was exposed to oxygen at 85 K. This procedure verifies for the absence of main contaminants on the platinum surface, which are residual carbon or CO and H<sub>2</sub> adsorbed from the residual gas in the UHV chamber. These sources of contamination will react with oxygen and form CO, CO<sub>2</sub> and H<sub>2</sub>O which desorb from the surface in temperature intervals 300-500 K, 200-350 K and 150-200 K, respectively. None of such desorption peaks were detected (Figure 2.6 b). A peak in the CO signal at 100 K is due to CO desorption from the filament. The same is true for a peak observed near 100 K for oxygen in Figure 2.6a.

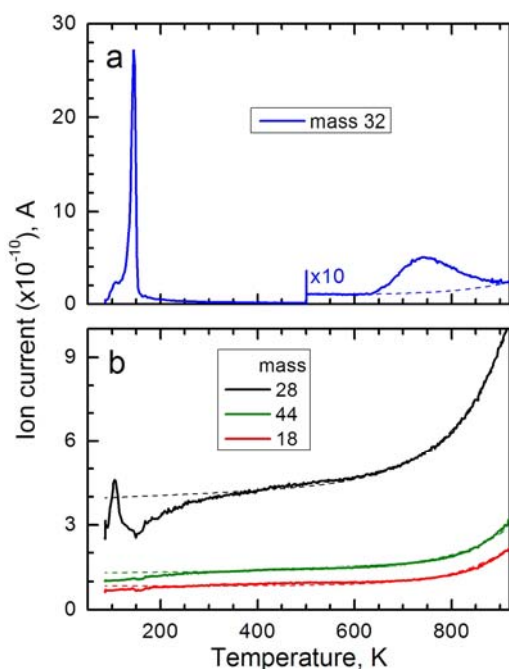


Figure 2.6 TPD traces of oxygen (a); carbon monoxide (mass 28), carbon dioxide (mass 44) and water (mass 18) (b) recorded after Pt(111) surface has been exposed to oxygen at 85 K. The dotted line shows the fit for the background signals calculated by formula (2.20)

All three masses in Figure 2.6b demonstrate a gradual increase with temperature. This is ascribed to increased heat transfer from the filament to the manipulator, which stimulates desorption of condensed residual gas and therefore increases the partial pressure of these molecules. From Figure 2.6b one can see that above 300 K the increase of the background signal can be fitted with the formula:

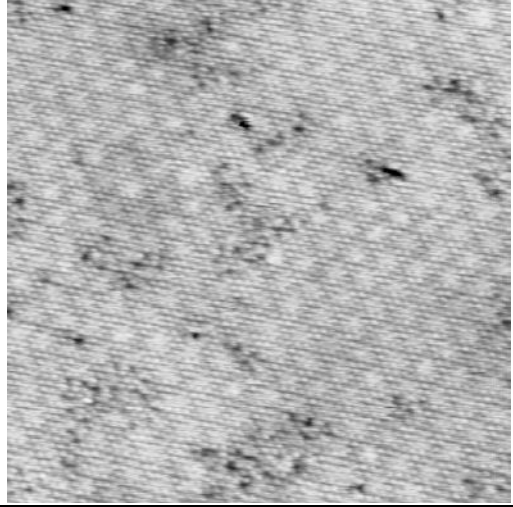
$$Bg(T) = C \exp(T) + BT + A, \quad (2.20)$$

where C, B, and A are fitting parameters. This formula is used in Chapter 3 to subtract the background signal from the oxygen TPD spectra.

#### References:

- [1] P. W. Palmberg, G. E. Riach, R. E. Weber, and N. C. MacDonald, Handbook of Auger Electron Spectroscopy, Physical Electronics Industries, Inc., Minneapolis, 1972.
- [2] K. W. Kolasinski, Surface Science: Foundation of Catalysis and Nanoscience, Wiley, West Chester, 2008.
- [3] F. Jona, J. J. A. Strozier, and W. S. Yang, Reports on Progress in Physics 45 (1982) 527.
- [4] K. Heinz and L. Hammer, The Journal of Physical Chemistry B 108 (2004) 14579.
- [5] F. Besenbacher, Reports on Progress in Physics 59 (1996) 1737.
- [6] C. J. Chen, Introduction to Scanning Tunneling Microscopy, Oxford University Press, New York, 2008.
- [7] S. Ernst, S. Wirth, M. Rams, V. Dolocan, and F. Steglich, Science and Technology of Advanced Materials 8 (2007) 347.
- [8] C. Bombis and H. Ibach, Surface Science 564 (2004) 201.
- [9] Single crystals supplied by Surface Preparation Laboratory (<http://www.surface-prep-lab.com/>)
- [10] J. W. Niemantsverdriet, Spectroscopy in Catalysis: An introduction, Wiley-VCH Verlag GmbH, Eindhoven, 2000.
- [11] D. A. King, Surface Science 47 (1975) 384.
- [12] A. M. de Jong and J. W. Niemantsverdriet, Surface Science 233 (1990) 355.





---

## Chapter 3

### Subsurface oxygen on Pt(111)<sup>1</sup>

---

<sup>1</sup>This chapter is based on: D.L. Bashlakov, L.B.F. Juurlink, M.T.M. Koper and A.I. Yanson, *Catal. Lett.* **142**, 1-6 (2011).

### 3.1 Introduction

Platinum is a primary catalyst for many oxidation reactions from fuel cells to automotive exhausts. The industrial and technological importance is reflected in the efforts by the scientific community to understand the interaction between the platinum surface and gas phase oxygen over the last four decades [1-11]. Although this effort has yielded a wealth of information, we show in this chapter that even the most intensely studied system, O<sub>2</sub>/Pt(111), can still yield surprising results that affect our view of the catalytic action under realistic conditions.

Studies of the interaction of the Pt(111) surface with molecular oxygen under UHV conditions show that if dosed at temperatures below 100 K, O<sub>2</sub> adsorbs molecularly into the  $(\sqrt{3}/2 \times \sqrt{3}/2)R15^\circ$  structure and a 0.44 ML O<sub>2</sub> per Pt coverage. When temperature increases, adsorbed O<sub>2</sub> partially desorbs and partially dissociates into chemisorbed atomic oxygen. While the desorbing O<sub>2</sub> signal appears at 150 K during TPD measurements [1, 2, 4, 6], remaining atomic oxygen forms the p(2x2) structure on the surface, clearly visible by LEED [6]. This adsorbed atomic oxygen recombinatively desorbs at much higher temperatures with a maximum near 750 K on TPD spectra [1, 2, 4, 6].

The p(2x2) structure obtained by dissociating molecularly bound O<sub>2</sub> can also be obtained by dosing O<sub>2</sub> at room temperature [6, 8-10]. It has been shown that the dissociative adsorption of molecular oxygen on Pt(111) requires two next nearest unoccupied fcc threefold-hollow sites [11]. This limits the maximum coverage of a well-ordered overlayer to 0.25 ML of atomic oxygen, where O occupies every fourth fcc site [9, 10]. This overlayer has been extensively studied with UHV techniques and is often used as a starting point in studies of oxidation reactions on Pt(111) [3-5, 7-10, 12-14].

In contrast to O<sub>2</sub>, other oxygen sources require only one fcc site for dissociation [15]. Therefore, coverages up to 0.75 ML of atomic oxygen can be achieved by dissociation of NO<sub>2</sub> on Pt(111) at 400 K [3, 16-18]. Even higher coverages (up to 2.5-2.9 ML) can be produced by exposure to more aggressive oxidants, such as ozone [19] and atomic oxygen [20, 21]. In combination with DFT calculations, it has been shown that oxygen adsorption on Pt(111) up to the coverage of 0.4-0.5 ML precedes the growth of a thicker platinum oxide layer [22-24].

Recently, a number of groups have combined preparation of single crystal or polycrystalline samples in UHV with reactivity studies at the



relatively high pressure of (up to) 1 atm. Under these conditions, a thin layer of platinum oxide forms on the surface in the temperature range of 450-600 K [25]. Furthermore, apparently the platinum oxide surface has a higher turnover rate for CO oxidation than the metallic surface [26]. This oxide has been identified by X-ray diffraction as  $\alpha$ -PtO<sub>2</sub> [27, 28] which decomposes at temperatures between 700 and 800 K [29]. These results differ from those obtained in UHV studies as no oxide formation has been observed on platinum in a similar temperature range [1, 4, 6, 30-32]. It is also opportune to note that the formation of platinum “oxide” state has been reported previously, albeit at considerably higher temperatures (900-1100 K) [33]. The same authors, however, had shortly thereafter re-assigned this effect to the oxidation of Si impurities in their platinum single crystals [34].

In this work we show that the 0.25 ML coverage limit for O<sub>2</sub> dissociative adsorption on Pt(111) can be overcome even at high vacuum conditions, if oxygen exposure is conducted in the catalytically relevant temperature range 400-600 K. Our results indicate that oxygen adsorbs not only on the surface, but also migrates to the sub-surface region, so that additional oxygen is stored underneath the conventional 0.25 ML surface layer. While this subsurface oxygen has lower reactivity towards CO oxidation, its presence does not alter the reactivity of the surface-bound oxygen layer.

### 3.2 Experimental section

Experiments were performed with two separate UHV systems using two Pt(111) single crystals. The detailed description of these systems and the procedures for Pt(111) surface preparation was given in the previous chapter. The Pt(111) samples were exposed to O<sub>2</sub> (Messer 5.0) and CO (Air Liquide 4.7) by background dosing at  $3\text{-}6 \times 10^{-7}$  and  $1 \times 10^{-8}$  mbar, respectively. For every individual TPD measurement, Ar sputtering and annealing the crystal to 1200 K in vacuum preceded oxygen adsorption in the Lionfish UHV instrument. In the Omicron UHV system, the crystal surface was checked by STM in every experiment prior to O<sub>2</sub> adsorption. Only when atomic resolution of a clean surface was achieved, the sample was transferred to the preparation chamber, exposed to O<sub>2</sub> and placed back in the STM stage.

The quarter monolayer atomic O coverage at 300 K was used as a calibration for the amount of desorbed oxygen during the TPDs, and as a reference structure for the LEED and STM measurements. All results were

obtained by exposing a clean Pt(111) surface to 400 L of molecular O<sub>2</sub> at various temperatures, and to 2.2 L of CO at 90 K unless noted otherwise (1 L= 1x10<sup>-6</sup> Torr-s). In all measurements O<sub>2</sub> dosing was stopped and system was pumped down before cooling the crystal.

### 3.3 Results and discussion

#### 3.3.1. Oxygen adsorption at various temperatures

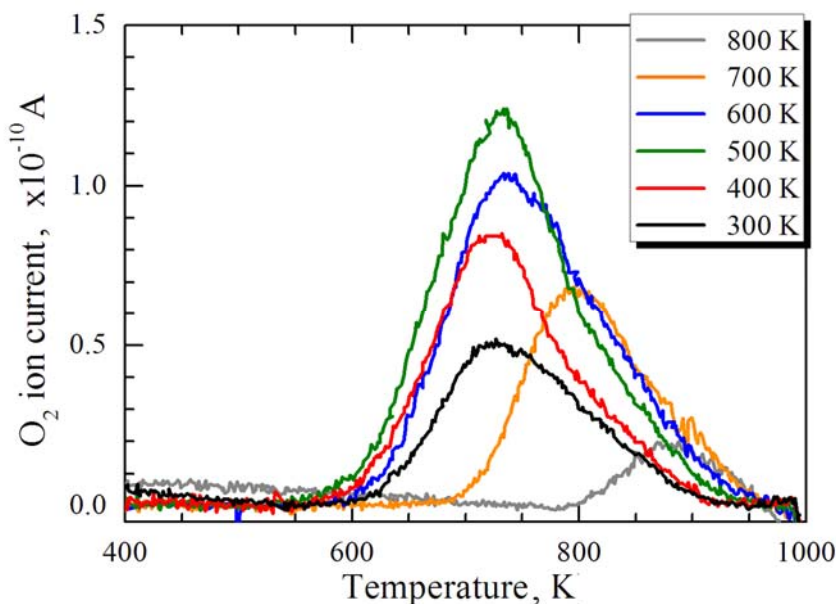


Figure 3.1. O<sub>2</sub> TPD spectra of Pt(111) exposed to 400 L O<sub>2</sub> at various temperatures taken at 2 K/s heating rate. All spectra have been corrected for rising backgrounds at higher temperatures using formula (2.20).

Figure 3.1 shows TPD spectra obtained after exposing the Pt(111) surface to 400 L O<sub>2</sub> at different temperatures in the range 300-800 K. As the peak areas in these spectra are a direct measure of the amount of O adsorbed on the surface prior to the temperature ramp, it is clear that this amount depends non-linearly on the temperature at which the surface was exposed to O<sub>2</sub>. The TPD peak area increases with substrate temperature up to 500 K, and rapidly drops for higher dosing temperatures. Higher dosing temperatures induce an upward shift in the maximum desorption temperature. As the onset of O<sub>2</sub> recombinant desorption lies at ~600 K,

dosing oxygen at temperatures above 600 K simply leads to concomitant O<sub>2</sub> desorption from the surface.

Figure 3.2a shows the integrated TPD peak areas versus adsorption temperature. The error bars reflect one standard deviation obtained from multiple TPD measurements convoluted with the estimated error resulting from background subtraction. The black line only serves to guide the eye.

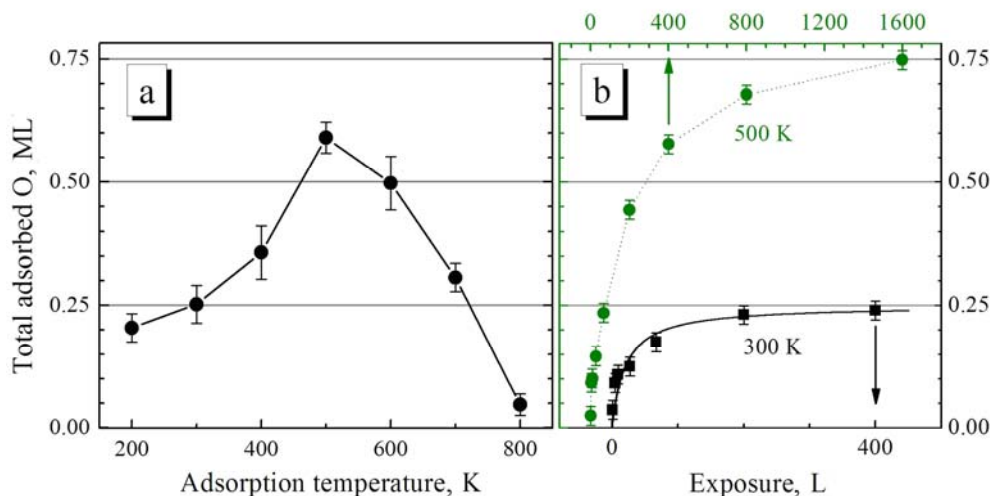


Figure 3.2 a) Amount of adsorbed O as a function of adsorption temperature after the exposure of Pt(111) to 400 L of oxygen. b) The O uptake curve for dosing at 300 K (squares) and 500 K (circles).

The area of the TPD peaks is normalized to saturation coverage of atomic oxygen obtained at 300 K as shown in Figure 3.2b (black squares). The data points were fitted with an uptake curve calculated from the adsorption rate for Langmuirian dissociative adsorption:

$$\frac{d\delta}{dt} = s_0 f (1 - \delta)^2, \quad (3.1)$$

where  $\delta$  equals the relative coverage,  $s_0$  is the initial sticking probability, and  $f$  is the normalized flux of molecules to the surface. Equation (3.1) can be transformed into a simple differential equation:

$$-\frac{d(1 - \delta)}{dt} = f s_0 (1 - \delta)^2, \quad (3.2)$$

which has a solution:

$$\delta = \frac{s_0 ft}{s_0 ft + 1} \cdot (3.3)$$

By definition,  $\delta = \frac{\theta}{\theta_{SAT}}$  where  $\theta$  is absolute coverage and  $\theta_{SAT}$  is saturation coverage of adsorbents in the ML, and product of flux  $f$  and time  $t$  gives the exposure  $L$ . Thereby, expression (3.3) transforms into:

$$\theta = \theta_{SAT} \frac{s_0 L}{s_0 L + 1} \cdot (3.4)$$

The black line in Figure 3.2b is calculated from (3.4) for an initial sticking probability  $s_0=0.05$  and  $\theta_{SAT}=0.25$  ML. It shows that exposure of Pt(111) to 400 L of O<sub>2</sub> results in (near) saturation for oxidation at 300K.

Figure 3.2a demonstrates that by increasing the substrate temperature, the total amount of adsorbed O on Pt(111) can be at least twice as high as the 0.25 ML obtained for oxidation at 300K. This result seems to be at odds with most results from previous UHV experiments as 0.25 ML was considered the maximum coverage when dosing molecular oxygen on Pt(111) [8-10, 13, 14]. However, the result is simultaneously not surprising considering recent reports of formation of an oxide layer on platinum single crystals and polycrystalline platinum during oxidation at atmospheric pressures (0.1-1 bar) in the temperature range 420-650 K [27, 28, 35]. Also, Derry and Ross reported a similar observation for Pt(111) and Pt(100) surfaces [36]. In their studies, platinum surfaces were exposed to ~40 L and ~3000 L O<sub>2</sub> at 370 K and 570 K respectively. While in the former case they obtained a coverage of ~0.2 ML, in the latter the amount of adsorbed oxygen was reported 3-5 times higher, which is very similar to our observations for Pt(111). We must also note that if we significantly increase the dose of O<sub>2</sub> at 500 K, the desorption signal will exceed the ~0.5 ML, as shown for the O uptake curve on Figure 3.2b (green circles). We conclude that even at UHV conditions oxygen dosing well above room temperature allows the Pt(111) surface to take up considerably more than the equivalent of 0.25 ML of atomic oxygen.

In this light it is interesting to note that the exposure of platinum to 400 L O<sub>2</sub> at 700 K leads to the adsorption of roughly the same amount of oxygen as exposure at 300 K, albeit with a significantly different desorption profile. In Figure 3.3, we show both TPD traces as red and green lines, respectively. However, unlike the 0.25 ML oxygen covered surface created at 300 K, the surface with the same coverage created at 700 K remains

active toward further oxygen adsorption when cooled back to room temperature. To demonstrate this, the surface was first exposed to 400 L of O<sub>2</sub> at 700 K, then cooled to room temperature and exposed to the same amount of oxygen again at 300 K. The consecutively recorded TPD trace is shown as a black line in Figure 3.3. The TPD peak area for the 700+300 K dose corresponds to an O coverage of 0.48 ( $\pm 0.04$ ) ML. As 0.25 ML is the maximum coverage that can be obtained for dissociation of O<sub>2</sub> at 300 K, we conclude that during the initial high-temperature exposure, oxygen is adsorbed in positions that do not block sites for consecutive dissociative adsorption of O<sub>2</sub> at 300 K.

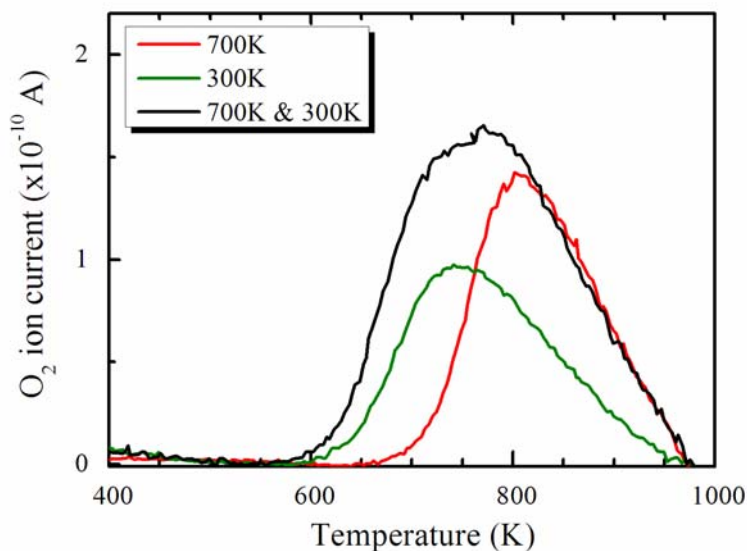


Figure 3.3 TPD spectra of oxygen adsorbed at 300K (green line) and 700K (red line) on clean Pt(111) and of oxygen dosed at 700 K and 300 K consecutively (black line). Heating rate is 4 K/s.

Enhanced oxygen coverage was previously obtained on Pt(111) in a number of TPD studies in which NO<sub>2</sub>, O<sub>3</sub> or O were used as the source of atomically adsorbed oxygen [19, 21, 37]. For low doses, oxygen adsorbs into the same p(2x2) structure as for O<sub>2</sub> dosing at room temperature [8, 17, 37]. Higher doses lead to the formation of p(2x1) domains with a local 0.5 ML coverage [17]. TPD traces from these higher coverages show an additional O<sub>2</sub> desorption peak at 500 K. The lower desorption temperature is suggested to result from repulsive interaction between oxygen atoms in the p(2x1) domains [21, 22, 37]. Our data in Figures 3.1 and 3.3 do not show an

additional peak at 500 K, even at oxygen coverage corresponding to  $\sim 0.5$  ML. Instead, we observe an increase in the peak intensity at 710 K. These observations indicate that the oxygen-loaded surface resulting from exposure to  $O_2$  at higher temperatures is different from the  $p(2 \times 1)$  overlayers observed in the  $O/O_3/NO_2$  experiments.

### 3.3.2. Surface structure

To investigate the surface structure of these high oxygen-covered platinum surfaces, we use LEED and STM. Figure 3.4 shows LEED patterns for Pt(111) exposed to  $O_2$  at 300 (a), 500 (b) and 700 K (c). Diffraction spots resulting from the clean Pt(111) surface are encircled. Although considerably weaker in Figure 3.4c, all three images show an additional diffraction pattern that corresponds to a  $(2 \times 2)$  structure [8]. We note that the Pt(111) surface covered mostly with  $p(2 \times 1)$  oxygen domains yields a similar LEED pattern, while having twice the amount of oxygen on the surface [20, 21, 37]. Therefore, using LEED alone we cannot unambiguously identify the structure.

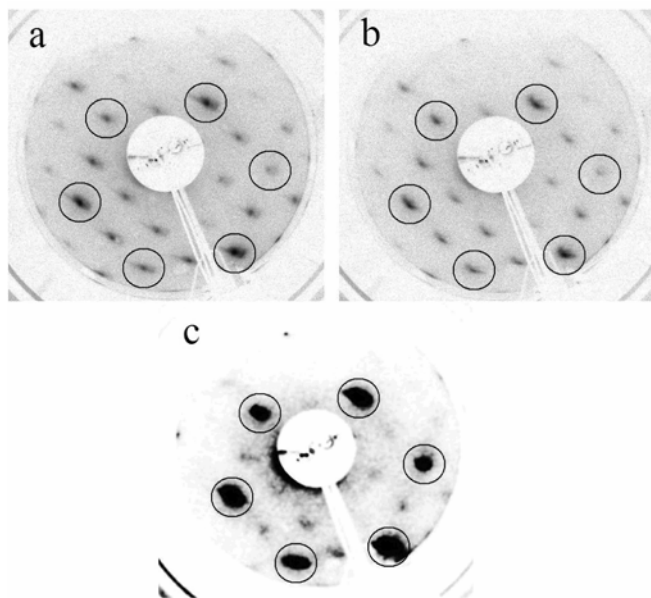


*Figure 3.4. LEED images for the Pt (111) surface exposed to 400 L of  $O_2$  at (a) 300 K, (b) 500 K and (c) 700 K. All images were recorded at 100 eV incident electron beam energy and a sample temperature of 85 K. Image in panel (c) was digitally enhanced to reveal the weak  $(2 \times 2)$  oxygen diffraction spots.*

To visualize the surface structure locally, we have performed STM topography measurements. Images in Figure 3.5 were obtained for oxygen adsorbed on Pt(111) at 300 K (a) and 500±50 K (b). Figures 3.5a and 3.5b both show the same p(2x2) structure of 0.25 ML of adsorbed atomic oxygen known from previous STM studies [13, 14]. This means that, although TPD data in Figure 3.2 show that the amount of oxygen adsorbed at 500 K is twice that for 300 K, it is not found in the top layer. Therefore we are left to conclude that additional oxygen created by exposure to O<sub>2</sub> at elevated temperatures is stored *below* the surface of the metal. We note that contrary to the reported step-edge facilitated oxidation on Rh(111) at elevated temperatures [38], our STM study did not reveal surface buckling near the step edges corresponding to oxide growth [39]. We would like to emphasize that by using the term “subsurface oxygen” we refer only to the location of this additional oxygen. We prefer to avoid the terms “subsurface oxide” or “bulk oxide” prior the additional studies of a surface structure, despite that oxides exist for most of the transition metals [40, 41]. Finally, we note that the strongly faded (2x2) diffraction pattern observed after dosing oxygen at elevated temperatures (Figure 3.4c) may result from small amounts of O remaining at the surface or from a (2x2) structure of O in subsurface sites.

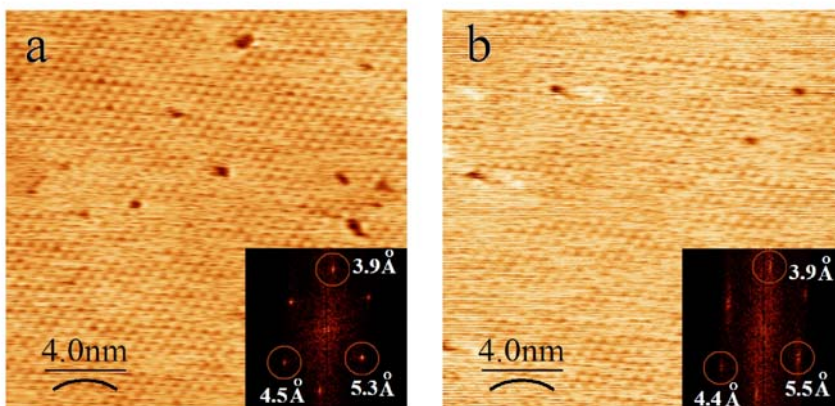


*Figure 3.5 17x17 nm<sup>2</sup> STM topography images with fast Fourier transformation (FFT) insets for Pt(111) exposed to 400 L of O<sub>2</sub> at room temperature (a, 0.13 nA, 0.18 V) and at 500±50 K (b, 0.12nA, 0.1 V). Distortion in the hexagonal order, which appears as a difference in the inter-atomic distance in the FFT insets, is due to drift always present in our STM.*

### 3.3.3. Oxygen reactivity towards CO oxidation

An unusual reactivity of the additional adsorbed atomic oxygen would support the subsurface oxygen hypothesis. To this end we have carried temperature programmed reaction (TPR) measurements to check how oxygen adsorbed on Pt(111) at various temperatures reacts with carbon monoxide. From previous studies it is known that the 0.25 ML of atomic oxygen on Pt(111) does not react with CO at temperatures below 150 K [5, 7]. CO and O co-adsorb in a 1:1 [42, 43] ratio and an increase in surface temperature activates the reaction that produces CO<sub>2</sub>. It has also been shown that covering the Pt(111) surface with atomic oxygen above 0.25 ML blocks adsorption of carbon monoxide [12, 44].

For the TPR traces shown in Figure 3.6, CO was adsorbed at  $\leq 90$  K onto the Pt(111) surface pre-exposed to O<sub>2</sub> at different temperatures. Subsequently, the sample temperature was ramped up while recording the partial pressures of  $m/e = 32$  (O<sub>2</sub>), 28 (CO) and 44 (CO<sub>2</sub>). In line with previous studies [5, 7, 42, 43], we observe that for the surface saturated with O at 300 K, all CO as well as most of the oxygen react to form CO<sub>2</sub>. However, when the surface is initially oxidized at 500 K, some amount of CO as well as O<sub>2</sub> are left on the surface after the same amount of CO<sub>2</sub> has been formed. At 700 K, even more CO desorbs at the expense of the CO<sub>2</sub> formation. This is most unusual: we seem to have both O and CO on platinum surface, yet they refuse to react even at elevated temperatures! Similar to our observation, Xu et. al. [45] reported the presence of unreactive isolated oxygen on the Pt(111) surface exposed to O<sub>2</sub> at 600 K. This clearly indicates that part of the atomic O created by high temperature adsorption is not available for CO oxidation. Considering that unreacted CO desorbs at lower temperatures than unreacted O, these findings support our claim that the additional oxygen is absorbed in subsurface sites.

The observation that some oxygen remains unreacted even when CO is available on the surface and the temperature favors the oxidation reaction, suggests that sub-surface oxygen is thermodynamically quite stable even in the absence of oxygen in the top layer. Rotermund *et al.* [46] already suggested thermodynamically stable subsurface oxygen to explain a change in work function for Pt(100) when the oxygen-covered surface was heated from 360 to 600 K. Furthermore, they observed desorption of the subsurface oxygen at 760 K, which is lower but comparable to what we observe for



Pt(111), and the reactivity of subsurface O towards CO oxidation similar to ours [47].

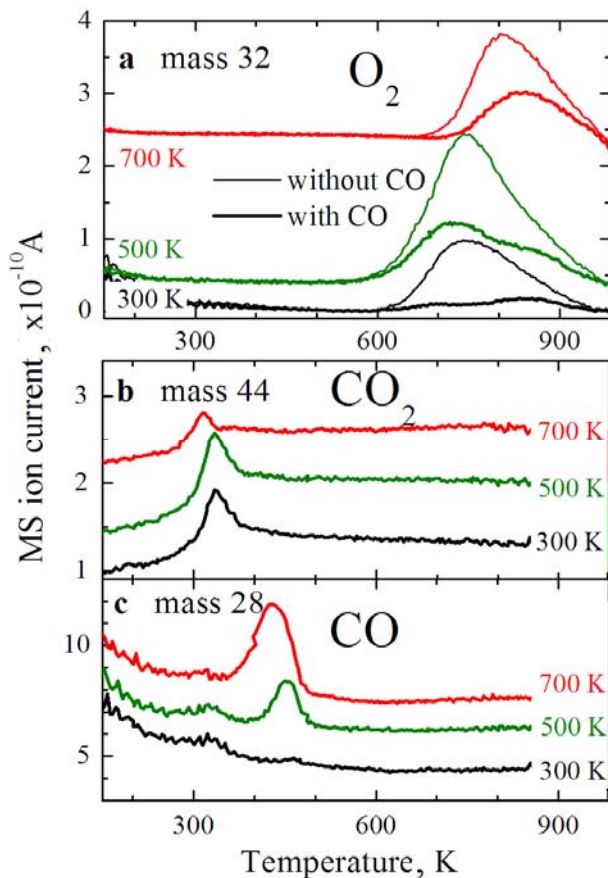


Figure 3.6 TPR spectra for a) O<sub>2</sub> b) CO<sub>2</sub> and c) CO recorded after CO adsorption on Pt(111), pre-exposed to O<sub>2</sub> at different temperatures. Figure 6a contains TPD traces of O<sub>2</sub> for comparison. Heating rate is 4 K/s. Graphs are offset vertically for clarity.

### 3.3.4. $^{16}\text{O}/^{18}\text{O}$ isotope exchange

Finally, we have carried out initial experiments with isotopically labeled  $\text{O}_2$ , to investigate the exchange between subsurface and surface oxygen. Experiments were performed as described for the data presented in Figure 3.3, with the difference that  $^{18}\text{O}_2$  was dosed at 700 K and  $^{16}\text{O}_2$  was used for subsequent dosing at 300 K. The results of the subsequent TPD are shown in Figure 3.7. It is obvious from the  $^{16}\text{O}^{18}\text{O}$  (mass 34) TPD trace that there is significant exchange between subsurface  $^{18}\text{O}$  (adsorbed at 700K) and overlayer  $^{16}\text{O}$  during desorption. At the same time, desorption for mass 36 starts at slightly higher temperature. This suggests that there is a lack of  $^{18}\text{O}$  in the p(2x2) layer for the associative desorption at the beginning. Apparently,  $^{18}\text{O}_2$  only desorbs when enough subsurface  $^{18}\text{O}$  has migrated up to the surface to occupy next nearest fcc sites. This also supports the idea that subsurface oxygen is stable without a p(2x2) overlayer present during cooling under UHV conditions. As only some exchange between the top and the subsurface oxygen layers is observed, this appears not to be a very fast process.

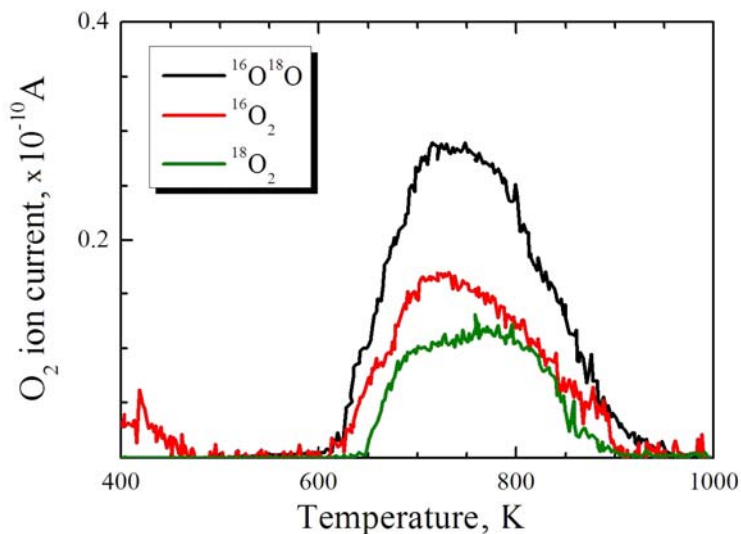


Figure 3.7. TPD spectra for 400L of  $^{16}\text{O}_2$  adsorbed at 300K on Pt (111) pre-exposed to 400L of  $^{18}\text{O}_2$  at 700 K. The heating rate is 2 K/s.

### 3.4 Conclusions

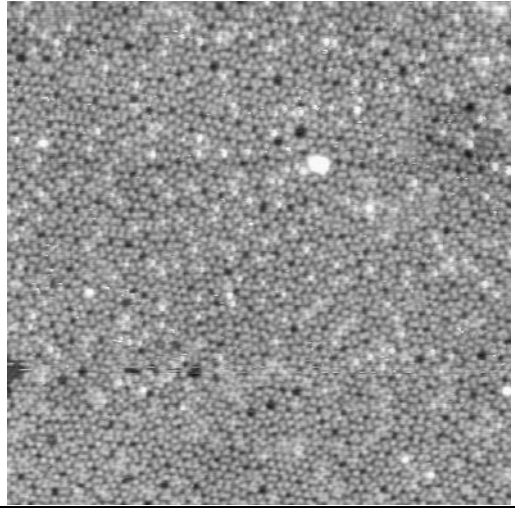
The Pt(111) surface, when exposed to molecular oxygen at elevated temperatures (400-600 K), can dissociatively adsorb more oxygen than the previously assumed limit of 0.25 ML. While we show that this total amount can significantly exceed 1/4 of a monolayer, we find only 0.25 ML present on the surface. This makes us conclude that excess oxygen is stored below the surface of platinum. Its desorption temperature is equal to or higher than that of surface-bound oxygen, making it quite stable even in the absence of the latter. While non-reactive on its own, this sub-surface oxygen layer has no negative effect on the catalytic surface reactivity of platinum towards CO oxidation under conditions studied. This sub-surface oxygen is likely the precursor of the stoichiometric  $\alpha$ -PtO<sub>2</sub> formed in catalytic reactors [27, 28] and as such provides an extra link between our understanding of catalytic oxidation reactions in UHV and in high pressure conditions.

## References:

- [1] H. Steininger, S. Lehwald, and H. Ibach, *Surface Science* 123 (1982) 1.
- [2] N. R. Avery, *Chemical Physics Letters* 96 (1983) 371.
- [3] D. Dahlgren and J. C. Hemminger, *Surface Science* 123 (1982) L739.
- [4] J. L. Gland, *Surface Science* 93 (1980) 487.
- [5] J. L. Gland and E. B. Kollin, *Surface Science* 151 (1985) 260.
- [6] J. L. Gland, B. A. Sexton, and G. B. Fisher, *Surface Science* 95 (1980) 587.
- [7] M. Kinne, T. Fuhrmann, J. F. Zhu, C. M. Whelan, R. Denecke, and H. P. Steinruck, *The Journal of Chemical Physics* 120 (2004) 7113.
- [8] N. Materer, U. Starke, A. Barbieri, R. Döll, K. Heinz, M. A. Van Hove, and G. A. Somorjai, *Surface Science* 325 (1995) 207.
- [9] K. Mortensen, C. Klink, F. Jensen, F. Besenbacher, and I. Stensgaard, *Surface Science* 220 (1989) L701.
- [10] P. R. Norton, J. A. Davies, and T. E. Jackman, *Surface Science* 122 (1982) L593.
- [11] J. Wintterlin, R. Schuster, and G. Ertl, *Physical Review Letters* 77 (1996) 123.
- [12] K. Mudiyansele, C.-W. Yi, and J. n. Szanyi, *The Journal of Physical Chemistry C* 113 (2009) 5766.
- [13] S. Volkening, K. Bedurftig, K. Jacobi, J. Wintterlin, and G. Ertl, *Physical Review Letters* 83 (1999) 2672.
- [14] J. Wintterlin, S. Volkening, T. V. W. Janssens, T. Zambelli, and G. Ertl, *Science* 278 (1997) 1931.
- [15] M. E. Bartram, R. G. Windham, and B. E. Koel, *Langmuir* 4 (1988) 240.
- [16] M. E. Bartram, R. G. Windham, and B. E. Koel, *Surface Science* 184 (1987) 57.
- [17] S. P. Devarajan, J. A. Hinojosa Jr, and J. F. Weaver, *Surface Science* 602 (2008) 3116.
- [18] D. I. Jerdev, J. Kim, M. Batzill, and B. E. Koel, *Surface Science* 498 (2002) L91.
- [19] N. A. Saliba, Y. L. Tsai, C. Panja, and B. E. Koel, *Surface Science* 419 (1999) 79.
- [20] C. R. Parkinson, M. Walker, and C. F. McConville, *Surface Science* 545 (2003) 19.
- [21] J. F. Weaver, J.-J. Chen, and A. L. Gerrard, *Surface Science* 592 (2005) 83.
- [22] J. M. Hawkins, J. F. Weaver, and A. Asthagiri, *Physical Review B* 79 (2009) 125434.
- [23] P. Légaré, *Surface Science* 580 (2005) 137.
- [24] H. Tang, A. Van der Ven, and B. L. Trout, *Physical Review B* 70 (2004) 045420.

- [25] M. S. Chen, Y. Cai, Z. Yan, K. K. Gath, S. Axnanda, and D. W. Goodman, *Surface Science* 601 (2007) 5326.
- [26] B. L. M. Hendriksen and J. W. M. Frenken, *Physical Review Letters* 89 (2002) 046101.
- [27] M. D. Ackermann, T. M. Pedersen, B. L. M. Hendriksen, O. Robach, S. C. Bobaru, I. Popa, C. Quiros, H. Kim, B. Hammer, S. Ferrer, and J. W. M. Frenken, *Physical Review Letters* 95 (2005) 255505.
- [28] C. Ellinger, A. Stierle, I. K. Robinson, A. Nefedov, and H. Dosch, *Journal of Physics-Condensed Matter* 20 (2008) 5.
- [29] L. Maya, E. W. Hagaman, R. K. Williams, G. D. Del Cul, and J. N. Fiedor, *The Journal of Physical Chemistry B* 102 (1998) 1951.
- [30] H. P. Bonzel and R. Ku, *Surface Science* 40 (1973) 85.
- [31] C. T. Campbell, G. Ertl, H. Kuipers, and J. Segner, *Surface Science* 107 (1981) 220.
- [32] P. Nolan, *The Journal of Chemical Physics* 111 (1999) 3696.
- [33] H. Niehus and G. Comsa, *Surface Science* 93 (1980) L147.
- [34] H. Niehus and G. Comsa, *Surface Science Letters* 102 (1981) L14.
- [35] A. K. Galwey, P. Gray, J. F. Griffiths, and S. M. Hasko, *Nature* 313 (1985) 668.
- [36] G. N. Derry and P. N. Ross, *Surface Science* 140 (1984) 165.
- [37] D. H. Parker, M. E. Bartram, and B. E. Koel, *Surface Science* 217 (1989) 489.
- [38] J. Klikovits, M. Schmid, L. R. Merte, P. Varga, R. Westerström, A. Resta, J. N. Andersen, J. Gustafson, A. Mikkelsen, E. Lundgren, F. Mittendorfer, and G. Kresse, *Physical Review Letters* 101 (2008) 266104.
- [39] J. G. Wang, W. X. Li, M. Borg, J. Gustafson, A. Mikkelsen, T. M. Pedersen, E. Lundgren, J. Weissenrieder, J. Klikovits, M. Schmid, B. Hammer, and J. N. Andersen, *Physical Review Letters* 95 (2005) 256102.
- [40] E. Lundgren and et al., *Journal of Physics: Condensed Matter* 18 (2006) R481.
- [41] M. Todorova, W. X. Li, M. V. Ganduglia-Pirovano, C. Stampfl, K. Reuter, and M. Scheffler, *Physical Review Letters* 89 (2002) 096103.
- [42] K. Bleakley and P. Hu, *Journal of the American Chemical Society* 121 (1999) 7644.
- [43] W. X. Li and B. Hammer, *Chemical Physics Letters* 409 (2005) 1.
- [44] A. L. Gerrard and J. F. Weaver, *The Journal of Chemical Physics* 123 (2005) 224703.
- [45] M. Xu, J. Liu, and F. Zaera, *The Journal of Chemical Physics* 104 (1996) 8825.
- [46] H. H. Rotermund, J. Lauterbach, and G. Haas, *Applied Physics A: Materials Science* 57 (1993) 507.
- [47] J. Lauterbach, K. Asakura, and H. H. Rotermund, *Surface Science* 313 (1994) 52.





## **Chapter 4**

### **Carbon monoxide oxidation on the Pt(111) surface at room temperature: STM and LEED studies**

## 4.1 Introduction

The most important application of platinum as a catalyst is in the three-way catalytic convertor used in automobile exhaust systems [1]. Platinum is also considered a potential work horse in fuel cell vehicles, where chemical energy of a fuel is converted directly into electricity. A major obstacle for development of platinum-based low temperature fuel cells is poisoning (blocking) of active sites on the catalyst by impurities or strongly-bound reaction intermediates. Carbon monoxide is the most common example of such “poison”. The answer to the question “What chemistry occurs on the active (platinum) surface at the atomic scale?” under more realistic conditions may provide clues how the real catalyst can be modified to prevent poisoning.

Intensive fundamental studies of the interaction of platinum with carbon monoxide and oxygen started in the 1970’s with the development of surface science [2]. Numerous experimental techniques [3-14] were used to gather information regarding surface structures, adsorption positions, and energies of adsorbed species on platinum. These were supported by theoretical calculations [15, 16]. When summarizing the literature available for CO and O on the Pt(111) surface, we obtain the following picture.

Adsorption of carbon monoxide on the Pt(111) surface depends on the CO pressure and on exposure time [8, 13]. The least densely ordered structure,  $(\sqrt{3}\times\sqrt{3})R30^\circ$ , contains 1/3 ML of CO adsorbed on top of platinum atoms. Further adsorption leads to the more densely ordered  $c(4\times 2)$  structure with 0.5 ML coverage where one half of CO molecules remains on top positions and the other half occupies bridge sites. Both commensurate structures were achieved at high vacuum conditions. An exposure of the surface to a higher CO pressure leads to the formation of an incommensurate layer ( $>0.5$  ML) [6, 9].

At room temperature oxygen adsorbs dissociatively on clean Pt (111) via a molecular precursor [4, 17]. In this process two oxygen atoms have to be separated by two interatomic distances to complete the dissociation. After dissociation, the oxygen atoms occupy face cubic centered hollow sites [11, 18]. This leads to the formation of the  $p(2\times 2)$  structure of atomic oxygen with 0.25 ML coverage [10, 12]. This structure is open for CO co-adsorption, thus a reaction to form  $\text{CO}_2$  can proceed [7, 19, 20].

Steady state oxidation of carbon monoxide on Pt(111) has been studied at temperatures above 350 K [3, 21, 22]. It was shown that the



surface reveals two states characterized by a high and a low reaction rate, depending on the composition of the O<sub>2</sub>:CO gas mixture and the surface temperature [22, 23]. Blocking (“poisoning”) of platinum by a CO adlayer was found to be responsible for the low reactivity regime. Lowering the concentration of carbon monoxide in the gas phase or increasing the sample temperature led to a distortion of the CO layer. This allowed molecular oxygen to find free sites needed for dissociation and the platinum surface switches to the high reaction state. This state is characterized by the presence of atomic oxygen on the surface [23, 24] and a sufficiently high CO→CO<sub>2</sub> conversion rate preventing surface poisoning. In contrast to steady state experiments, studies at room temperature and below were performed with a titration method, where the active Pt-O overlayer was replaced by a Pt-CO layer via the O<sub>ads</sub>+CO<sub>ads</sub>→CO<sub>2</sub> surface reaction [20, 25-27].

Despite abundant literature concerning ensemble-averaged studies of carbon monoxide oxidation on platinum, to date only one group had performed STM studies of this reaction at the atomic scale [26, 27], and only in a titration-type experiment. Furthermore, there is very little information available on the steady state oxidation reaction of CO on platinum at room temperature. In this chapter, we use STM and LEED techniques to visualize the processes on the Pt(111) surface in contact with various O<sub>2</sub>:CO gas mixtures at room temperature. While LEED provides us with structural information over a large surface area, STM shows what happens locally at the atomic scale for the same conditions. Our study shows that the Pt(111) surface remains active toward CO oxidation at room temperature for CO concentrations ≤ 0.3%. STM reveals the formation of a complex surface structure under reactive conditions where islands of adsorbed atomic oxygen are separated by disordered areas. These topographic measurements are complemented by LEED patterns, showing the presence of a (2x2) oxygen structure on the Pt(111) surface at the same conditions.

## 4.2 Experimental section

Experiments were performed using a commercial “Omicron” UHV system consisting of preparation and analysis (reaction) chambers with a base pressure of  $2 \times 10^{-10}$  mbar. The Pt single crystal (6mm diameter and 1mm thick) was cut and polished within 0.1° precision of the (111) plane on

one side. A detailed description of the system as well as the initial sample cleaning and STM tip preparation procedures can be found in Chapter 2. Daily cleaning procedures included annealing in  $3\text{-}4 \times 10^{-7}$  mbar of  $\text{O}_2$  for 30 min at 900 K with subsequent heating to 1000-1100 K in vacuum for several minutes. Afterwards, the sample was transferred to the reaction chamber which was kept at UHV.

A gas mixture with the required  $\text{O}_2\text{:CO}$  ratio was prepared in a separate mixing chamber equipped with a MKS121A Baratron capacitance manometer and leak valves. A schematic drawing of the dosing system is shown as an inset in Figure 4.1. This mixing chamber was separated from the reaction chamber via two valves with a small known volume in between. Dosing was performed by expansion of the prepared gas mixture from this small volume (3 mL, 1.2 Torr total pressure) into the reaction chamber (40 L). The latter was isolated from the pumps before gas mixture was admitted. It resulted in a total pressure of  $1 \times 10^{-4}$  mbar in the reaction chamber. The gases  $\text{O}_2$  (Messer 5.0) and  $\text{CO}$  (Air Liquide 4.7) were used as supplied.

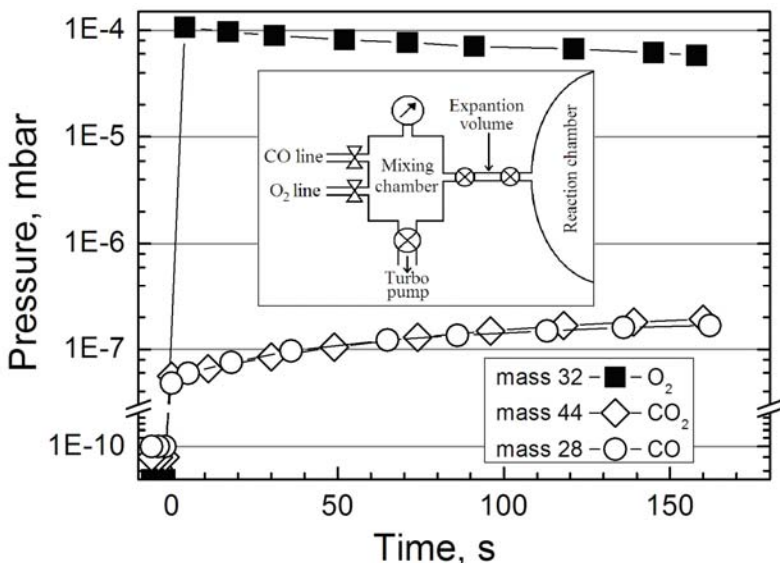


Figure 4.1 Evolution of the partial pressures in our deactivated reaction chamber after  $1 \times 10^{-4}$  mbar of oxygen was admitted at time=0 sec. The increase in the CO ( $\text{CO}_2$ ) partial pressure is due to the production of these gases by the mass spectrometer's filament.

Our experiments were carried out in a “batch reactor” mode, where the entire UHV was backfilled with the gas mixture and sealed for the duration of the measurement. Vibration sensitivity of the STM precluded using the turbo pump for steady state gas flow conditions. Furthermore, we had to refrain from using the sublimation and ion pumps in the reaction chamber during the experiments due to their high chemical activity towards the constituents of the O<sub>2</sub>:CO gas mixture. To keep the oxygen content stable, we had to deactivate titanium by keeping the analysis chamber under  $1 \times 10^{-4}$ - $1 \times 10^{-3}$  mbar of O<sub>2</sub> for several hours after every bake-out. It sufficiently reduced the pumping speed of titanium and allowed us to use the analysis chamber as a closed reaction volume. Figure 4.1 demonstrates the changes in the oxygen pressure after backfilling the deactivated reaction chamber.

Ideally, the changes in the gas composition should be caused only by the catalytic reaction on the sample. However, we have noticed the presence of an additional source of CO and CO<sub>2</sub> in our reaction chamber when oxygen was admitted. From Figure 4.1 one can see that the amount of CO increases gradually and seems to saturate eventually. The filament of the quadrupole mass spectrometer (QMS) was responsible for this, since we observe the increase in the CO and CO<sub>2</sub> signals only when this filament is turned on in presence of O<sub>2</sub>. Most probably, it is due to the oxidation of residual carbon present in the UHV chamber. Unlike the QMS filament, the LEED filament had no detectable influence on the contents of the gas mixture.

Mass spectrometry confirmed that the initial concentration of the admitted mixture of oxygen and carbon monoxide was the same as prepared in the mixing chamber. For example, dosing of the gas mixture with the smallest concentration of carbon monoxide used in our experiments (200:1 of O<sub>2</sub>:CO) resulted in the initial  $p_{\text{CO}} \approx 5 \times 10^{-7}$  mbar ( $P_{\text{TOTAL}} = 1 \times 10^{-4}$  mbar).

Time needed to resolve the surface structure with LEED was limited only by the frame rate chosen to record the video. Measuring sample topography with STM required more time. Several tens of raster lines had to be collected to resolve the surface structures on Pt(111) terraces. With a scanning speed of 122-166 nm/s and a frame size of 30x30 nm<sup>2</sup> it took ~100 sec to obtain a two-dimensional image of the surface. From Figure 4.1 one can see that the composition of the gas mixture remains approximately constant within this time frame. Therefore, we could register changes in the surface structure even if they were caused by the variation in the composition of the gas mixture due to the influence of the chamber/filament.

Sample-to-tip drift correction was applied while scanning the clean platinum surface prior to its exposure to the gas mixture. Fast Fourier Transform (FFT) analysis revealed the  $2.75\pm 0.2$  Å interatomic distance for the clean Pt(111) surface confirming proper calibration of the piezo scanner. The distance between the nearest platinum atoms (2.77 Å) was also used as a reference for determining the periodicity of adsorbed species from the LEED images. From the analysis of the positions of platinum diffraction spots we found that our sample was retracted 11-12 mm from the geometrical focus of the LEED apparatus. We have taken this into account in our LEED structure calculations for the adsorbed overlayers. More details on the adlayer periodicity calculations were provided in Chapter 2.

## 4.3 Results and discussion

### 4.3.1 STM and LEED

The clean Pt(111) surface was exposed to O<sub>2</sub> or to a O<sub>2</sub>:CO mixture of various compositions (10:1, 100:1 and 200:1) at  $P_{\text{TOTAL}}=1\times 10^{-4}$  mbar. Changes in the surface structure were observed with STM and LEED during the exposure. We have to note for clarity that STM and LEED data were collected during separate dosing events. By synchronizing the measurements to the start of exposure to gases, local changes in the STM topography were correlated with the development of the diffraction patterns.

When the platinum surface was exposed to pure oxygen, rapid formation of an ordered structure in both STM and LEED measurements was observed as shown in Figure 4.2a. The ordering can be identified as the p(2x2) overlayer of atomic oxygen with 0.25 ML coverage [10, 12, 27]. Analysis of the STM and LEED images indicated  $5.5\pm 0.35$  Å and  $5.3\pm 0.2$  Å as the distances between nearest oxygen atoms, respectively. This is twice the distance between nearest platinum atoms (2.77 Å). This demonstrates that the presence of residual CO in our system does not influence oxygen adsorption.

The topography data in Figure 4.2b show the development of a different adlayer after the introduction of a 10:1 (O<sub>2</sub>:CO) gas mixture. The diffraction data show exactly the same behavior where new patterns develop immediately after dosing. The orientation of these extra diffraction spots is rotated by 30° compared to the (1x1) diffraction features of the bare Pt(111) surface, indicating that the observed structure is formed by carbon

monoxide [6, 8]. The ordered structure on the topographic image in Figure 4.2b corresponds to a Moiré pattern formed by an incommensurate CO overlayer at this pressure [9]. The periodicity of the observed structure is  $8.6 \pm 1 \text{ \AA}$  as derived from the FFT analysis of the current and subsequent STM images. The period of the Moiré structure defined from the LEED images is  $8.0 \pm 0.6 \text{ \AA}$ . Evacuating the chamber allowed resolving the CO structure with a periodicity of  $3.7 \pm 0.1 \text{ \AA}$  [9, 28].

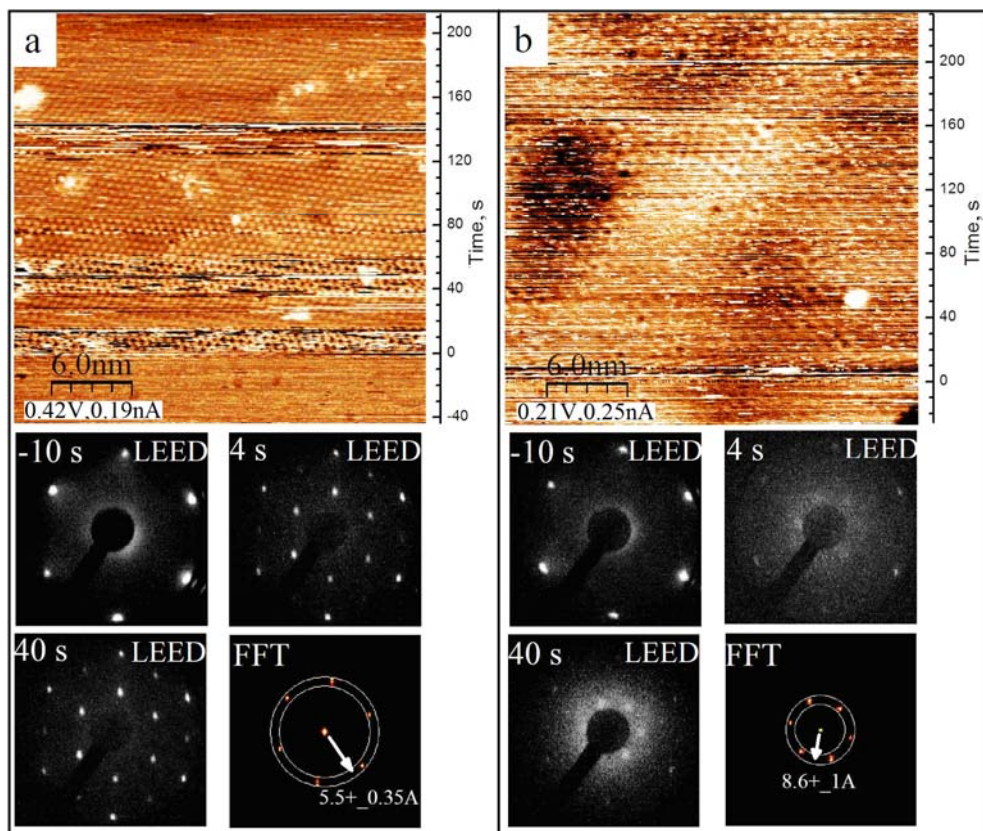
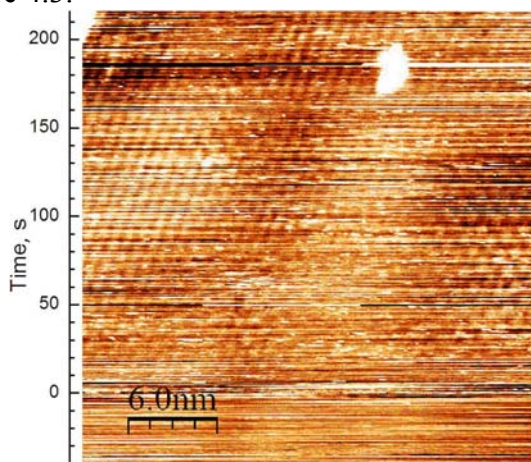


Figure 4.2. Changes in the surface structure of Pt(111) before and after exposure to clean oxygen (a), and a ( $\text{O}_2:\text{CO}$ ) 10:1 mixture (b), recorded with STM and LEED. LEED snapshots, taken at 66 eV primary electron beam energy, are shown for the clean platinum surface ( $t < 0$ ) and at certain times after gases were introduced into the reaction chamber. The bottom right images present FFT analyses of the STM data recorded after  $t = 0$ . Size of STM images is  $26 \times 26 \text{ nm}^2$ .

The Pt(111) surface adsorbs carbon monoxide faster than oxygen from the 10:1 mixture even though the number of CO molecules colliding with the surface is ten times smaller than for oxygen. This can be explained by the difference in the sticking probabilities ( $S_{CO}=0.8-0.9$  [5, 20],  $S_{O_2}=0.06$  [4, 14]) and the amount of available adsorption sites on Pt(111) for these gases. The clean platinum surface at room temperature can accommodate only 0.25 ML of oxygen but twice the amount of CO (0.5-0.68 ML depending on the CO pressure) [9, 12]. Even if some oxygen molecules are able to find a place to dissociate immediately after the clean surface has been exposed to the gas mixture, they will be removed by adsorbed CO through formation of  $CO_2$ . Carbon monoxide will continue to dominate over oxygen for the adsorption position on the surface until no suitable sites for  $O_2$  dissociation are left. Apparently, this happens so fast that both in the STM and LEED the formation of the CO overlayer from this mixture looks like simple carbon monoxide adsorption. Indeed we observe that exposing the Pt(111) surface to  $1 \times 10^{-5}$  mbar of pure CO (same pressure as  $P_{CO}$  in the 10:1  $O_2$ :CO gas mixture) leads to a rapid development of the Moiré pattern as is shown in Figure 4.3.



*Figure 4.3 STM topography image of the Pt(111) surface  $26 \times 26 \text{ nm}^2$  taken during its exposure at  $t=0$  to  $1 \times 10^{-5}$  mbar of CO ( $V=0.21$  V,  $I=0.2$  nA).*

The effect of CO domination over oxygen on the platinum surface remains even for the 100:1 ( $O_2$ :CO) gas mixture as shown in Figure 4.4. The (2x2) oxygen structure forms immediately after the gases are introduced into the chamber and it takes a few seconds for CO to remove it. This means that oxygen has an initial advantage over carbon monoxide to adsorb on a clean platinum surface due to its higher concentration. The formed oxygen

adlayer is open for subsequent adsorption of CO [7, 19]. Further surface behavior is determined by the surface reaction and the competition of gas molecules for the available adsorption sites. A single reaction event clears up sites suitable only for the adsorption of carbon monoxide. Molecular oxygen, which adsorbs at room temperature only via dissociation, requires two adjacent surface sites which can only become available after the two nearest oxygen atoms recombine with CO molecules and leave the surface. The probability of such an event is determined by the amount and the type of molecules which arrive at the surface from the gas phase, i.e. the higher the CO content in the gas mixture, the higher the chance for CO to prevent O<sub>2</sub> dissociative adsorption. The concentration of carbon monoxide supplied from the 100:1 gas mixture to the platinum surface is apparently sufficient to poison the surface for oxygen dissociation. Thus, the diffraction patterns in Figure 4.4 show the development of the carbon monoxide overlayer with time.

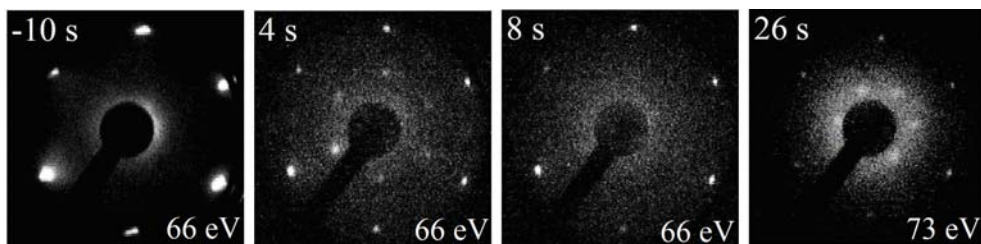


Figure 4.4. The snapshots of the LEED video recorded during the exposure of the Pt(111) surface to the 100:1 (O<sub>2</sub>:CO) gas mixture.

We noticed two types of behavior while dosing a 200:1 (O<sub>2</sub>:CO) mixture. The first type, shown in Figure 4.5a, has the same trends as for the 100:1 mixture but with a longer time needed for the formation of the CO overlayer. The topography data show first the formation of ordered oxygen islands which become disordered and then transform into the c(2x4) islands of CO. The second type, shown in Figure 4.5b, shows no switching to the carbon monoxide structure. The diffraction patterns of the p(2x2)-O adlayer become more pronounced with time. The STM image first shows the formation of patches of oxygen with disordered regions in between. The ordered oxygen layer is restored over the whole surface while the surface reaction reduces the CO concentration in the gas phase. We believe that the difference between these two cases is caused by the higher residual CO level in the reaction chamber for the first set of data, as will be shown below from the mass spectrometric data.



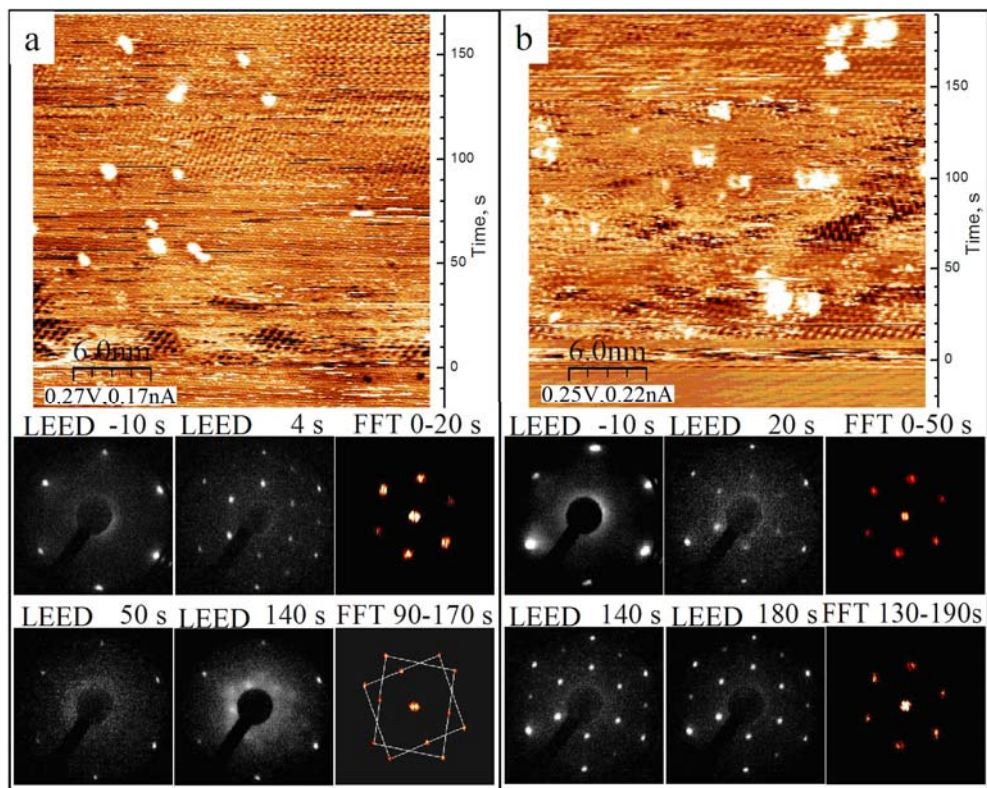


Figure 4.5 Changes in the surface structure of the Pt(111) exposed to the 200:1 ( $O_2$ :CO) mixture showing the formation of the CO overlayer (a) and preservation of the active Pt-O layer (b) recorded with STM and LEED. The zero point on the time scale (right side of STM images) indicates the moment gases were admitted to the reaction chamber. FFT analysis from the top part of the topographic image (a) shows the presence of two  $c(4 \times 2)$ -CO domains marked with squares. Size of STM images is  $26 \times 26 \text{ nm}^2$ . All LEED data were taken at 66 eV electron beam energy.

The results of topographic and diffraction measurements are summarized in Figure 4.6. The time periods during which the ordered CO layer or disordered surface were detected are marked with the black and gray bars, respectively. The white-hatched bars mark the time periods during which the  $(2 \times 2)$  ordering of oxygen was observed. The response of the Pt(111) surface to the exposure to the  $O_2$ :CO gas mixture can be divided in two steps. The first one describes the adsorption of the gases on the clean surface. This step is defined by the sticking probability of carbon monoxide ( $S_{CO}=0.8$ ) and the dissociative adsorption probability ( $S_{O_2}=0.06$ ) of oxygen



on Pt(111). Almost every molecule of carbon monoxide will adsorb upon collision with the platinum surface, while only 6% of the colliding oxygen molecules will adsorb and dissociate. That is why the p(2x2) oxygen structure develops only for gas mixtures with the CO concentration smaller than 10% ( $O_2:CO=10:1$ ).

The second step includes the reaction between the atomic oxygen and carbon monoxide on the surface. No reaction is expected for the 10:1 mixture since the surface is blocked for the dissociative adsorption of molecular oxygen. However, the platinum surface covered with oxygen remains open for CO adsorption. The further process is defined by the competition of the molecules from the gas phase for the sites available after a single reaction event took place. The STM images from Figure 4.5 show that this competition leads to clustering on the surface where the p(2x2)-O islands are separated by disordered regions. The disordered regions presumably consist mostly of carbon monoxide [25, 27], which partially (or totally) blocks dissociation of molecular oxygen, as the structured CO adlayer is formed only after the unstructured regions spread over the whole platinum surface, which is shown in Figure 4.6 with grey bars.

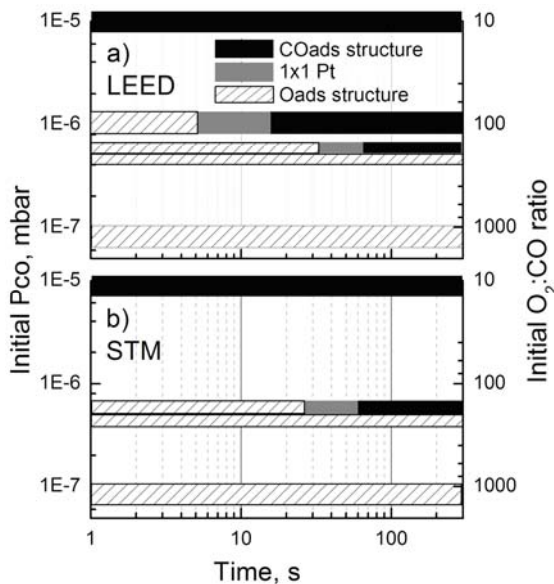


Figure 4.6 The time dependence for the adsorbate structures on the Pt(111) surface for different gas mixture compositions as observed with LEED (a) and STM (b) at a total gas pressure of  $1 \times 10^{-4}$  mbar. “1x1Pt” marks the region where no ordered structure of adsorbates was detected and only a diffraction pattern of Pt(111) was seen with LEED.

The energetically most stable adsorption site for carbon monoxide inside the ordered  $p(2 \times 2)$ -O layer is on top of platinum atoms next to oxygen (non-O-bonded platinum atoms) [7]. The adsorption energy for co-adsorbed CO is almost the same as for the clean surface [15]. Also, the presence of carbon monoxide on top of platinum atoms does not change the chemisorption energy of oxygen atoms [15]. According to Alavi et al. [16] the situation changes if CO is displaced from the equilibrium position to the bridge site. It weakens the oxygen bond to one of the platinum atoms. Since the reaction barrier is defined by the strength of oxygen bonding to the surface, it thereby reduces the barrier for the reaction. Carbon monoxide has to leave the energetically favorable equilibrium position inside the  $p(2 \times 2)$ -O overlayer to react. The situation is different on the periphery of oxygen islands. Carbon monoxide can already occupy the bridge sites in the oxygen free regions due to the higher concentration and the repulsive interaction between adsorbed CO molecules. It also can happen that the oxygen atoms are already displaced from these equilibrium three-hollow fcc sites due to thermal excitations. In both cases, the effective reaction barrier would be lower on the border of the  $p(2 \times 2)$ -O island than in its interior. Therefore the reaction is expected to be more efficient on the oxygen island periphery.

The difference in reactivity of oxygen in the interior of the  $p(2 \times 2)$  islands and at the borders was experimentally observed for the Pt(111) surface in oxygen titration experiments [25-27]. STM measurements carried out at 237-274 K showed that the reaction proceeds on the borders between ordered oxygen and carbon monoxide islands [26]. There it was also shown that some time (an induction period) needed for the formation of closely packed  $c(4 \times 2)$ . Nakai et al. [25] demonstrated two types of reaction kinetics for the same system. The first one was observed at 240 K when regions with high coverage of carbon monoxide coexist with the ordered oxygen islands, which was also confirmed by fast XPS [19]. In this case, the reaction takes place at the island's periphery in agreement with STM studies. The second type of reaction kinetics was observed at 350 K, where carbon monoxide accumulated on the surface only after oxygen had been removed. It was explained by thermally induced disordering of the  $p(2 \times 2)$ -O islands [29]. However, the partial pressure of carbon monoxide in their experiments was rather low ( $P_{CO} = 1 \times 10^{-8}$  mbar), and so it is quite possible that CO was removed by reaction with atomic oxygen faster than it was supplied from the gas phase, so that a two-phase interface could not be established. Wintterlin et al. [27] had to apply a CO pressure of  $5 \times 10^{-8}$  mbar at much

lower temperature (244 K) to form the  $c(4 \times 2)$ -CO patches on the oxygen-free platinum surface. In the oxygen titration experiments of Campbell et al. [3] at 320 K with a molecular beam intensity corresponding to a CO pressure of  $1 \times 10^{-7}$  mbar, carbon monoxide was effectively removed by the surface reaction as fast as it was supplied to the surface.

Our STM results show that a densely packed carbon monoxide adlayer forms after the oxygen islands have disappeared (Figure 4.5a). This observation differs from previous STM studies at lower temperatures [26, 27] where both the  $c(4 \times 2)$ -CO and  $p(2 \times 2)$ -O structures were present on the surface simultaneously. It must be noted that the temperature used in our studies is closer to the desorption temperature of the  $c(4 \times 2)$ -CO layer. The TPD peak starts around 300K [5, 6]. The potential energy surface is relatively flat for CO diffusion on Pt(111) [30, 31]. A one third monolayer of CO forms the ordered  $(\sqrt{3} \times \sqrt{3})R30^\circ$  structure at 150 K where the CO molecules are on top of every third platinum as shown by Hopster and Ibach [8]. On the other hand, some amount ( $\sim 0.1$  ML) of the bridge sites was found to be occupied by carbon monoxide at 275 K even before the coverage reached  $1/3$  ML [32]. Therefore, under our conditions carbon monoxide can freely migrate on Pt(111) and approach oxygen atoms for reaction before the formation of the densely packed CO adlayer. Another difference is that we have both reactants present in the gas phase. Competitive adsorption is taking place inside the disordered regions and at their borders. Disordered regions will turn into a CO or oxygen covered surface with time (Figure 4.5), depending on the (changes in the)  $O_2:CO$  mixture composition.

#### 4.3.2 Mass spectrometry

Using the reaction chamber as a closed vessel solved the problem of vibrations for the STM measurements. Yet if we look at the time evolution of the  $O_2:CO$  ratio in the gas mixture (Figure 4.7), the influence of the reaction chamber on the partial pressure of the reactants becomes noticeable. Oxidation of residual carbon by the filament of the mass spectrometer appears as a decrease in the  $O_2:CO$  mixture composition (increase in the CO partial pressure, cf. Figure 4.1) with time. Therefore the filament of the mass spectrometer was turned off shortly after the reaction mixture was introduced, and turned on again at the end ( $\Delta, \nabla$  datasets with dashed lines). From Figure 4.7c one can see that this preserves the active

state of the surface and the amount of initially admitted CO reduces significantly until the filament is switched back on. Keeping the filament of the mass-spectrometer on for the 200:1 gas mixture resulted in surface passivation at 30 sec ( $\square$  dataset).

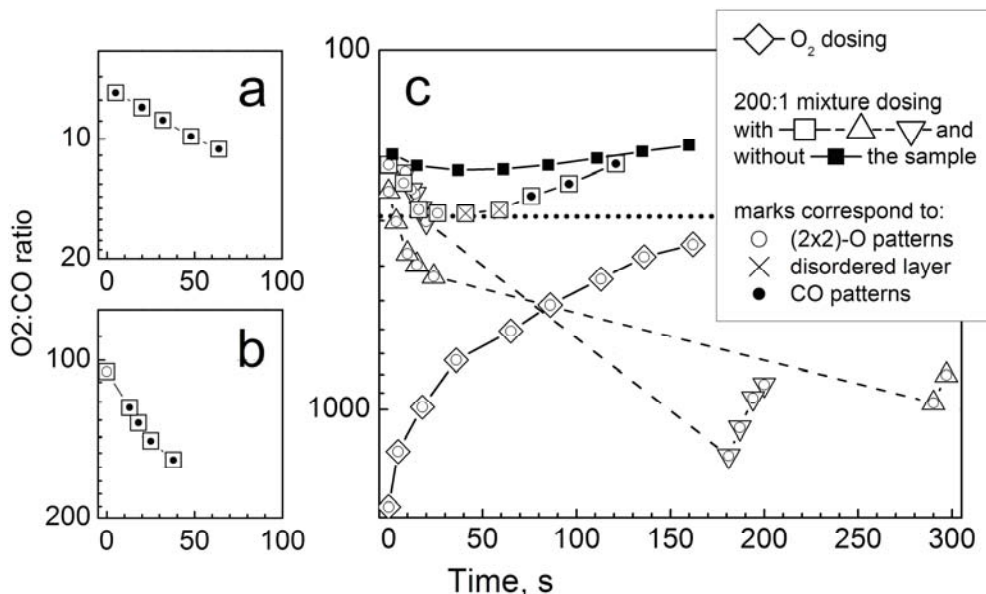


Figure 4.7 Changes in the  $O_2:CO$  gas mixture composition with time during the LEED measurements for the 10:1 mixture (a), 100:1 mixture (b), 200:1 mixture ( $\nabla$ ,  $\Delta$ ,  $\square$ ) and clean oxygen ( $\diamond$ ) (c) admitted into the reaction chamber.  $P_{total}=1 \times 10^{-4}$  mbar. Data points marked with ( $\circ$ ) correspond to the (2x2)-O LEED patterns. Diffraction patterns of the CO overlayer and unstructured surface adlayer (only (1x1) Pt(111) pattern visible) are marked with ( $\bullet$ ) and ( $\times$ ) symbols, respectively. The dataset with solid squares ( $\blacksquare$ ) shows the evolution of the 200:1 gas mixture admitted into the reaction chamber without the sample. The dashed lines mark the time when the filament of the mass spectrometer was off.

Even so, we can clearly see that at certain composition of the gas mixture the active state of the platinum surface changes drastically. The dotted horizontal line marks the concentration of carbon monoxide which splits the graph in two regions. At higher concentrations CO tends to accumulate on the surface, in time forming a compact layer which blocks the dissociation of molecular oxygen and deactivates the catalyst. The active state of the surface covered by atomic oxygen is restored if the

concentration of CO is kept below 0.3 %. It is opportune to note that an extrapolation of data from Ehsasi et al. to our experimental temperature and pressure regime gives a very similar value for the concentration of CO at which the transition from high to low reactivity was observed [22].

#### 4.3.3 Effect of CO poisoning on oxygen adsorption

Additional STM measurements were carried out to observe the effect of CO poisoning on oxygen adsorption on the Pt(111) surface. At the start of an experiment, the reaction chamber was filled with  $2\text{-}3 \times 10^{-7}$  mbar of carbon monoxide to form the CO adlayer on the surface. The total pressure in the chamber was then increased to  $1 \times 10^{-4}$  mbar by dosing oxygen. Such a dosing sequence results in a more than 300 times higher partial pressure of  $\text{O}_2$  than of CO. This  $\text{O}_2\text{:CO}$  ratio is below the poisoning level for a clean platinum surface, according to the previous mass spectrometry data (Figure 4.7).

The adlayer structure was monitored continuously by scanning the same surface region before and after the  $\text{O}_2$  admission and results are presented in Figure 4.8. As one can see no changes in the surface structure occur at the moment the surface was exposed to oxygen ( $t=0$ ). Noticeable changes in the CO layer appear as a vanishing of the ordered structure after  $\approx 550$  seconds. The signature of oxygen presence appears even later (800-850 sec). The topography of this state is similar to what has been observed in Figure 4.5 in the transition period: small fractions of the oxygen-covered surface separated with disordered regions of carbon monoxide. This layer transforms rapidly into the complete layer of atomic oxygen.

Dissociation of oxygen is one of the elementary steps in oxidation reactions (see equations 1.1-1.3 for example). The presented data demonstrate that dissociation is inhibited by the presence of CO on the surface, which is in line with previous studies [23]. Although some reaction is still taking place, since the CO layer gets replaced with time by the oxygen layer. Based on our measurements, we cannot say which sites remain active for CO oxidation, when most of the platinum surface is covered with CO. But it is obvious that the reactivity of the overall surface is quite low. It takes time to release CO from the (111) terraces so oxygen can adsorb. At the same time, we observe that transitions from the low reactive state into the high reactive one (Figure 4.8) and vice versa (Figure 4.5) have the same atomic scale mechanism. In both cases, the adsorbates

tend to form an island-like structure on the Pt(111) surface in the transition phase.

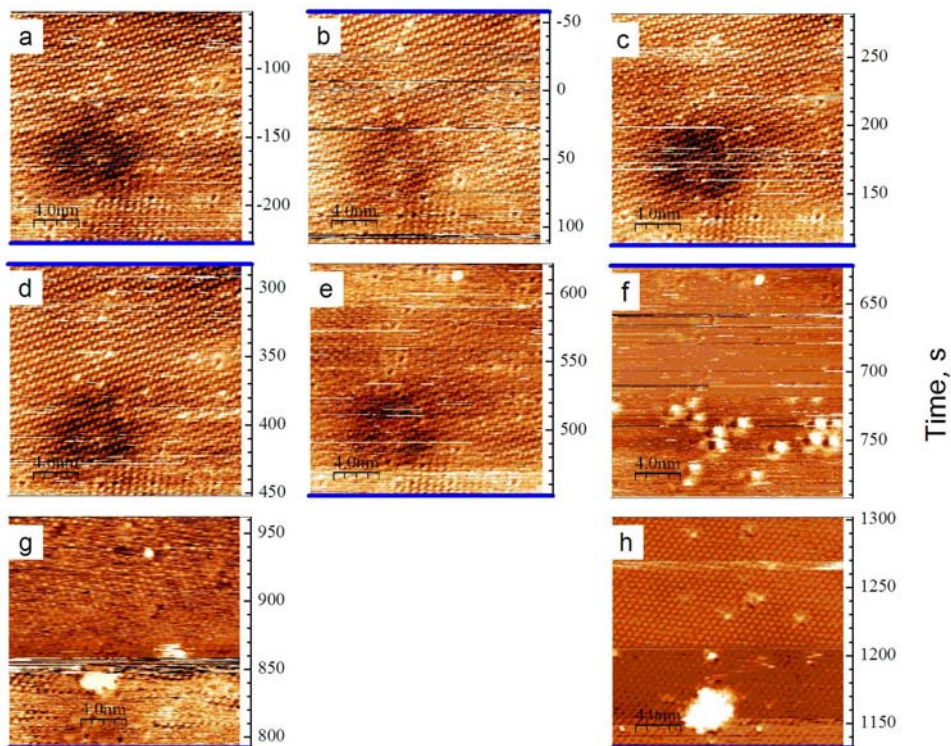


*Figure 4.8 Consecutive STM images of the same Pt(111) surface area pre-covered with CO before (a-b) and after (b-h) oxygen has been admitted into the reaction chamber (time scale shown on the left side of each image). Images a-g were collected at  $V=0.19V$  and  $I=0.2nA$  and image h recorded at  $V=0.35V$  and  $I=0.14nA$ . The moment  $1 \times 10^{-4}$  mbar of  $O_2$  was introduced to correspond to  $t=0$  sec (image b). Blue lines mark the first scan line of each topographic measurement. Voltage pulses have been applied to the tip to stabilize it after image (g) was recorded. Size of all images is  $17 \times 17 \text{ nm}^2$ .*

## 4.4 Conclusions

At room temperature and  $1 \times 10^{-4}$  mbar gas pressure the catalytic oxidation of CO on Pt(111) was found extremely sensitive to the composition of gas mixture. STM and LEED measurements combined with mass spectrometry demonstrate that CO present at concentration above  $\approx 0.3\%$  blocks the surface for the dissociative adsorption of oxygen, forming a dense ordered adlayer. At concentrations close to 0.3% carbon monoxide can be effectively converted into  $\text{CO}_2$  without poisoning the surface, while Pt(111) demonstrates a complex surface structure with islands of atomic oxygen coexisting with disordered regions of carbon monoxide. The presence of such structure suggests that the oxidation reaction proceeds at the border of the oxygen islands, in agreement with previous titration experiments [25, 26]. Finally, if the concentration of CO in the ( $\text{O}_2$ :CO) mixture is much less than 0.3%, the catalyst remains in its active state while its surface is covered with a compact  $p(2 \times 2)$  layer of atomic oxygen. At room temperature adsorbed oxygen does not go subsurface on Pt(111), nor introduces surface oxidation or restructuring of this surface [33, 34], and adsorbed CO forms a compact monolayer unperturbed by thermally-induced desorption. No oscillations between the high and low activity states are observed, while the finite lifetime of the transition phase may be interesting to investigate at higher pressures [9].

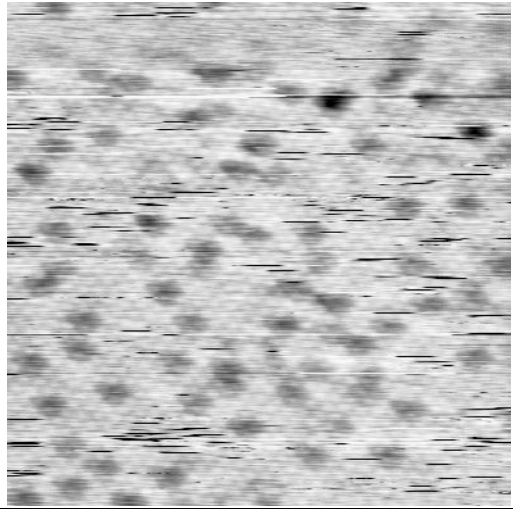
## References:

- [1] B. E. Nieuwenhuys, *Advances in Catalysis* 44 (1999) 259.
- [2] T. Engel and G. Ertl, *Advances in Catalysis* 28 (1979) 1.
- [3] C. T. Campbell, G. Ertl, H. Kuipers, and J. Segner, *The Journal of Chemical Physics* 73 (1980) 5862.
- [4] C. T. Campbell, G. Ertl, H. Kuipers, and J. Segner, *Surface Science* 107 (1981) 220.
- [5] C. T. Campbell, G. Ertl, H. Kuipers, and J. Segner, *Surface Science* 107 (1981) 207.
- [6] G. Ertl, M. Neumann, and K. M. Streit, *Surface Science* 64 (1977) 393.
- [7] J. L. Gland and E. B. Kollin, *Surface Science* 151 (1985) 260.
- [8] H. Hopster and H. Ibach, *Surface Science* 77 (1978) 109.
- [9] S. R. Longwitz, J. Schnadt, E. K. Vestergaard, R. T. Vang, I. Stensgaard, H. Brune, and F. Besenbacher, *The Journal of Physical Chemistry B* 108 (2004) 14497.
- [10] N. Materer, U. Starke, A. Barbieri, R. Doll, K. Heinz, M. A. Van Hove, and G. A. Somorjai, *Surface Science* 325 (1995) 207.
- [11] K. Mortensen, C. Klink, F. Jensen, F. Besenbacher, and I. Stensgaard, *Surface Science* 220 (1989) L701.
- [12] P. R. Norton, J. A. Davies, and T. E. Jackman, *Surface Science* 122 (1982) L593.
- [13] M. O. Pedersen, M.-L. Bocquet, P. Sautet, E. Legsgaard, I. Stensgaard, and F. Besenbacher, *Chemical Physics Letters* 299 (1999) 403.
- [14] Y. Y. Yeo, L. Vattuone, and D. A. King, *The Journal of Chemical Physics* 106 (1997) 392.
- [15] K. Bleakley and P. Hu, *Journal of the American Chemical Society* 121 (1999) 7644.
- [16] A. Alavi, P. Hu, T. Deutsch, P. L. Silvestrelli, and J. r. Hutter, *Physical Review Letters* 80 (1998) 3650.
- [17] B. C. Stipe, M. A. Rezaei, and W. Ho, *The Journal of Chemical Physics* 107 (1997) 6443.
- [18] J. Wintterlin, R. Schuster, and G. Ertl, *Physical Review Letters* 77 (1996) 123.
- [19] M. Kinne, T. Fuhrmann, J. F. Zhu, C. M. Whelan, R. Denecke, and H. P. Steinruck, *The Journal of Chemical Physics* 120 (2004) 7113.
- [20] F. Zaera, J. Liu, and M. Xu, *The Journal of Chemical Physics* 106 (1997) 4204.
- [21] H. Hopster, H. Ibach, and G. Comsa, *Journal of Catalysis* 46 (1977) 37.
- [22] M. Ehsasi, M. Matloch, O. Frank, J. H. Block, K. Christmann, F. S. Rys, and W. Hirschwald, *The Journal of Chemical Physics* 91 (1989) 4949.



- [23] M. Berdau, G. G. Yelenin, A. Karpowicz, M. Ehsasi, K. Christmann, and J. H. Block, *The Journal of Chemical Physics* 110 (1999) 11551.
- [24] J. H. Miners, S. Cerasari, V. Efstathiou, M. Kim, and D. P. Woodruff, *The Journal of Chemical Physics* 117 (2002) 885.
- [25] I. Nakai, H. Kondoh, K. Amemiya, M. Nagasaka, T. Shimada, R. Yokota, A. Nambu, and T. Ohta, *The Journal of Chemical Physics* 122 (2005) 134709.
- [26] S. Volkening and J. Wintterlin, *The Journal of Chemical Physics* 114 (2001) 6382.
- [27] J. Wintterlin, S. Volkening, T. V. W. Janssens, T. Zambelli, and G. Ertl, *Science* 278 (1997) 1931.
- [28] J. A. Jensen, K. B. Rider, M. Salmeron, and G. A. Somorjai, *Physical Review Letters* 80 (1998) 1228.
- [29] M. Nagasaka, H. Kondoh, I. Nakai, and T. Ohta, *The Journal of Chemical Physics* 122 (2005) 044715.
- [30] M. Lynch and P. Hu, *Surface Science* 458 (2000) 1.
- [31] E. Schweizer, B. N. J. Persson, M. Tushaus, D. Hoge, and A. M. Bradshaw, *Surface Science* 213 (1989) 49.
- [32] J. S. McEwen, S. H. Payne, H. J. Kreuzer, M. Kinne, R. Denecke, and H. P. Steinruck, *Surface Science* 545 (2003) 47.
- [33] D. Bashlakov, L. Juurlink, M. Koper, and A. Yanson, *Catalysis Letters* 142 (2012) 1.
- [34] C. Ellinger, A. Stierle, I. K. Robinson, A. Nefedov, and H. Dosch, *Journal of Physics-Condensed Matter* 20 (2008)





---

## **Chapter 5**

**Correlating surface activity and STM current transients during CO oxidation on Pt(111)**

## 5.1 Introduction

The tremendous spatial resolution of the scanning tunneling microscope (STM) makes this technique an effective tool for surface science studies. The visualization of the surface with atomic resolution has now become routine in many laboratories [1]. Topography measurements can be seen nowadays as a conventional application of STM. At the same time, not only spatial information but also information about surface dynamics can be obtained with STM. Binnig et al. were the first to demonstrate this application of STM [2]. They observed that migration of surface bound species under the tip causes a disturbance in the tunnel current. Later, it was shown that fluctuation of the tunnel current contains information on a variety of dynamic processes on the surface [3-7].

The majority of STM studies on dynamical systems have focused on the diffusion of surface bound species [6-14]. The transport of adatoms over an ordered substrate during which adsorbed species randomly jump between equilibrium adsorption sites is similar to Brownian motion. Such dynamics can be described in terms of a residence time in a single adsorption site,  $\tau$ , or a hopping rate between two sites,  $\nu=1/\tau$  [15]. The interest in adsorbate diffusion is caused by its importance to a number of technological processes, such as heterogeneous catalysis and epitaxial layer growth. In the case of catalysis, the ability to register each elementary step of the reaction separately may be considered as an ultimate goal for STM studies. These are adsorption, dissociation, diffusion, reaction and desorption of surface bound species.

Frame-by-frame imaging of a surface remains convenient in case of slow diffusion [8-10]. Due to the relatively long residence time of the adsorbate, its migration can be registered as the position change on two subsequent images. State of art STM systems developed in recent years are able to sample the surface with frequency of up to 100 frames per second [16, 17]. Despite this impressive performance, it remains a struggle to visualize the separate elementary steps even for a simple surface reaction such as CO oxidation [18]. Taking into account that the reaction rate for the single reaction site reaches  $1 \times 10^3$ - $1 \times 10^4$  events per second [19], the image

sampling speed should be two orders of magnitude higher for the conventional frame-by-frame approach to “see” the reaction.

An alternative approach for the study of surface dynamics is not based on visualization of atoms or molecules in space, but rather to follow them in time on a single location. The presence of adspecies causes changes in the local (electronic) density of states (LDOS), since they influence locally the electronic structure of the surface [20, 21]. Temporal changes in the LDOS due to dynamic processes cause corresponding alterations in the tip-sample tunnel barrier and changes in its conductivity (equation 2.14). Hence, motion of the surface bound species can be detected via fluctuations in the tunnel current [5, 11, 12]. It has been shown that the temporal resolution of such current fluctuation type measurements for modern STM instruments is three orders of magnitude better than the frame-by-frame method [11, 12].

Intrigued by the potential of the current fluctuation method, we have tried to apply it to CO oxidation over a platinum surface, bearing in mind that our final goal is to find the active surface sites for this reaction. Although this reaction is quite simple, it involves a number of elementary steps and each of these may be a potential source for current transients. Expecting contributions to the current fluctuations from adsorption, diffusion and recombination from both oxygen and carbon monoxide, we chose to use noise spectra of the tunnel current to quantify the current fluctuations.

## 5.2. Measurement approach and technique

The general thought which brought us to these noise spectra experiments is the following. Imagine two surface sites with different reactivity toward the CO+O reaction which are also continuously forming CO<sub>2</sub>. The reactants are supplied to each site via diffusion or adsorption. The amount of CO and O arriving at the reaction site determines the reaction rate of that particular site. The latter is valid for a high gas phase-to-surface supply of the reactants. The tunnel current between surface and tip suspended over either of the two sites will vary due to the changes in LDOS of the surface during each reaction event. Figure 5.1 schematically represents such a random fluctuation of tunnel current during CO<sub>2</sub> formation with the reaction rate for site **II** higher than for site **I**.

We choose to use fast Fourier transformation (FFT) of the current to quantify the intensity of the current fluctuations. Figure 5.1 (c) demonstrates

the magnitude of the FFT of both  $I(t)$  traces representing the noise spectra (frequency spectra of the current fluctuations) for each site. One can see that the intensity of the noise spectrum is higher in the case of a site with higher reactivity as reaction events are more frequent. The original idea of measuring noise included collecting noise spectra at every spot of the surface while recording the surface topography. In this way we expected to obtain a reactivity map of the catalytically active surface, similar to the diffusion map obtained by Lagoute et al. on Cu(100) [7].

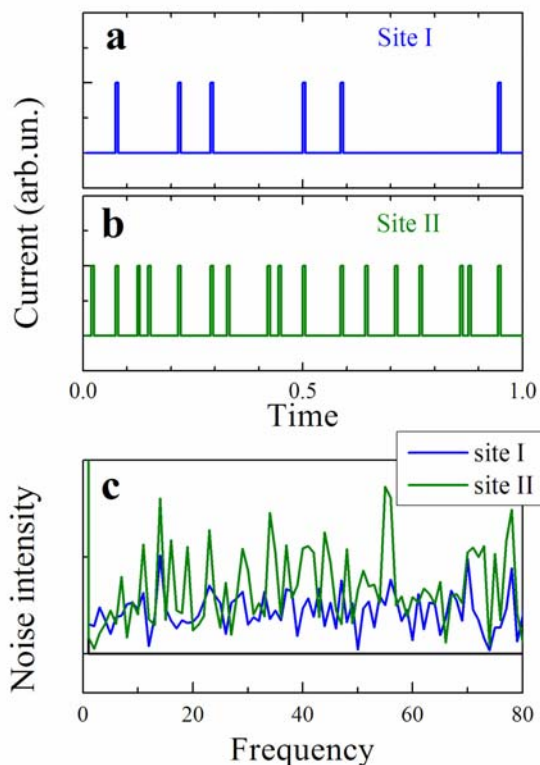


*Figure 5.1 Schematic representation of the tunnel current transient during the catalytic reaction on two sites with different reactivity (a, b) and corresponding noise spectra (c) obtained by FFT of  $I(t)$  dependences.*

Measurements of STM noise spectra were performed in the Omicron system (see Chapter 2 for description) by using the analysis chamber equipped with the STM stage as a closed reactor during the CO oxidation reaction. The Pt(111) sample kept at room temperature was used as the

catalytically active surface. Dosing of reactants was performed by admitting the reactant gases into the reaction chamber as is described in Chapter 4.

In order to validate the applicability of the proposed method, noise spectra were obtained while scanning the surface. For this purpose the tunnel current was sampled with a frequency of  $5 \times 10^5$  data points per second with a National Instruments DAC card (NI USB-6221 BNC). The collected array of data was converted with FFT into noise spectra. The tunnel current input for this measurement was taken from the  $I_{\text{tunnel}}$  monitor of the Omicron STM control unit. The monitored voltage of  $I_{\text{tunnel}}$  signal was obtained from the tunnel current passing via the I-V converter with  $10^8$  V/A conversion coefficient and was subsequently enhanced 20 times by the Preamplifier unit (last one is also the floating power supply of an I-V converter designed by Omicron). The tip height ( $Z$ ) was regulated during scanning with the analog feedback loop intended to keep a constant tunnel current. It led to partial suppression of the noise spectra intensity for frequencies  $< 200$  Hz. More detailed information on influence of the feedback loop on frequency spectra can be found in references 3, 7, 25, and references therein.

### 5.3 Experiment and results

Sets of noise spectra of the tunnel current were obtained for the Pt(111) surface exposed to carbon monoxide, oxygen and a mixture of both gases. Examples of noise spectra are shown in Figure 5.2. The broad peak in the 3-20 kHz region (pink area in Fig.5.2), which is present in each spectrum, is the characteristic feature of the I-V converter (black line). The nature of the numerous sharp peaks (best visible in the blue spectra) is not totally clear. They seem to appear as a result of parameters such as the exact way the sample is clamped in the STM stage, cars on the nearby road, walking of nearby colleagues, etc. In other words, we expect that vibrations at the system's resonant frequencies caused these peaks. They can hardly be related to dynamic processes on the surface, since similar peaks were observed while scanning the clean (bare) surface. The background noise spectrum (red line on Figure 5.2) was obtained by averaging over a number of spectra measured on the clean Pt(111) surface in separate experiments.

Noise spectra were measured on a freshly cleaned platinum surface several times to determine the noise level range in the studied system. The

tip was cleaned with the field emission treatment procedure and stabilized as described in Chapter 2 prior to every one of 9 separate runs of the background noise detection. Figure 5.2 demonstrates two of such spectra with minimum (blue) and maximum (green) noise level.

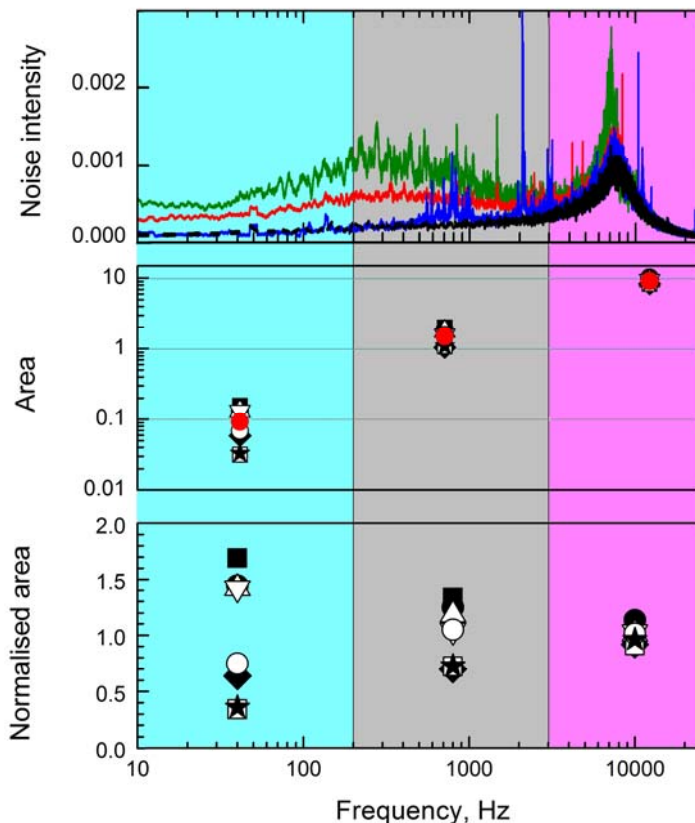


Figure 5.2 Determination of the background noise level. Top: the spectra obtained from the FFT of tunneling current: with zero current (amplifier noise – black line); lowest (blue) and highest (green) noise detected for bare platinum surface; noise spectrum averaged from 9 separate measurements (red). Middle: noise level calculated as the area under the noise spectra for 9 separate measurements (each marked with different symbol) for the frequency regions 0-200Hz (cyan), 200-3000Hz (gray) and 3-25 kHz (pink). Red symbols are an average over 9 spectra of the noise level. Bottom: deviation from the average noise level for the clean platinum surface.



The noise intensity for each spectrum was calculated as the surface area under the curve (Figure 5.2 (middle panel)). Three frequency bands were selected for analysis for the following reasons. The first band (0-200 Hz) is influenced by the feedback control of the STM electronics. Thus, the noise intensity in this region was partially suppressed. The last band (above 3 kHz) is affected by broadening of a frequency response for the I-V converter (broad peak). Only the 200-3000 Hz band seems to be unaffected by the instrument's performance. The average noise intensity was calculated for each band in order to normalize the range of the noise level of these bands. From the bottom graph of Figure 5.2 it is observed that the highest dispersion as well as the highest noise level is detected in the low frequency band, even though it is suppressed by the feedback loop.

Separate dosing of carbon monoxide and oxygen or a mixture of both gases was done to compare the noise spectra of the tunnel current without (Figures 5.3 and 5.4) and with (Figure 5.5) reaction proceeding on the surface. During carbon monoxide dosing, it was noticed that a certain period of time is needed for CO to form an ordered layer. The structure observed after this onset is shown in the right part of STM image. Scanning of this regular CO layer caused an appearance of two peaks at  $\approx 70$  Hz and  $\approx 250$  Hz in the noise spectra (not shown), as a result of the delay in the feedback loop response. No other differences in the noise intensity were observed between spectra from an ordered (90-120 s) as well as a disordered CO layers (0-90 s) and the bare Pt(111) surface.

The STM images on Figures 5.3-5.6 were rotated clockwise for better representation. Unlike the previous STM images, the scan lines are now vertical. In this way the observed topographical changes can be easily compared to the time scale of the noise intensity data. The noise data are plotted as the normalized area under the noise spectra in the three frequency windows introduced in Figure 5.2 and shown as data points at the exact times at which the tunneling current datasets were collected.

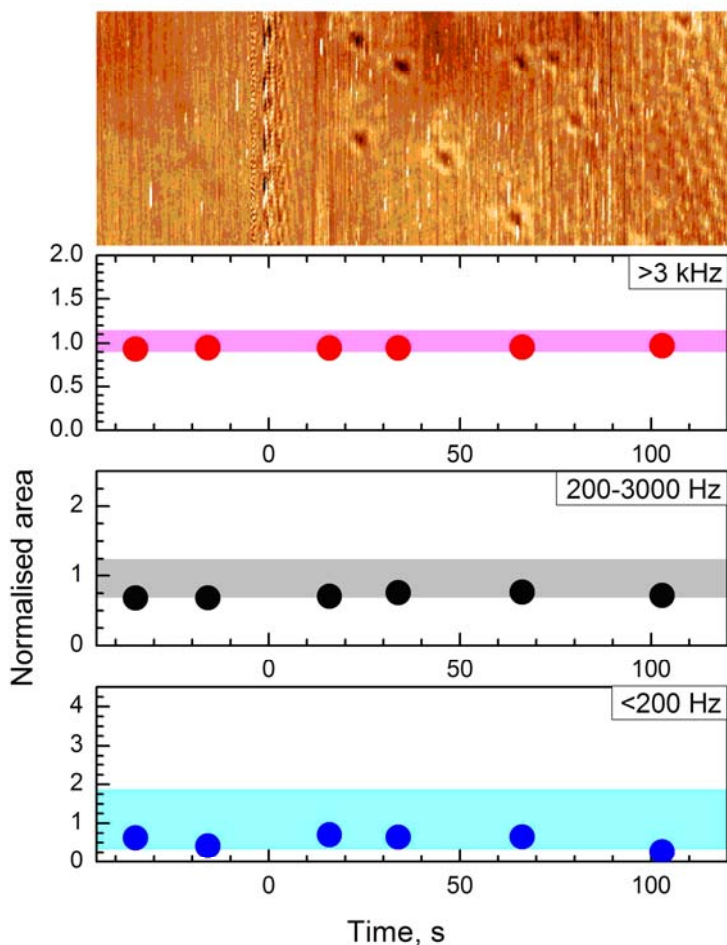


Figure 5.3 Topography of Pt(111) ( $17 \times 7 \text{ nm}^2$ ,  $I=0.2 \text{ nA}$ ,  $V=0.2 \text{ V}$ ) recorded while the surface is exposed to  $2\text{-}3 \times 10^7 \text{ mbar}$  of carbon monoxide. Circles show the noise level (normalized area) obtained for the three frequency windows. Bars are marking the noise level regions for the bare surface in the same frequency windows.

The dosing of  $O_2$  at  $1 \times 10^{-4}$  mbar led to the fast formation of a  $p(2 \times 2)$  layer of atomic oxygen as shown in the STM image in Figure 5.4. At the same time an increase in the noise intensity was observed for a number of spectra in the 0-200 and 200-3000 Hz windows. The same increase in the magnitude of the noise spectra was observed when platinum was exposed to the mixture of oxygen and carbon monoxide (Figure 5.5).

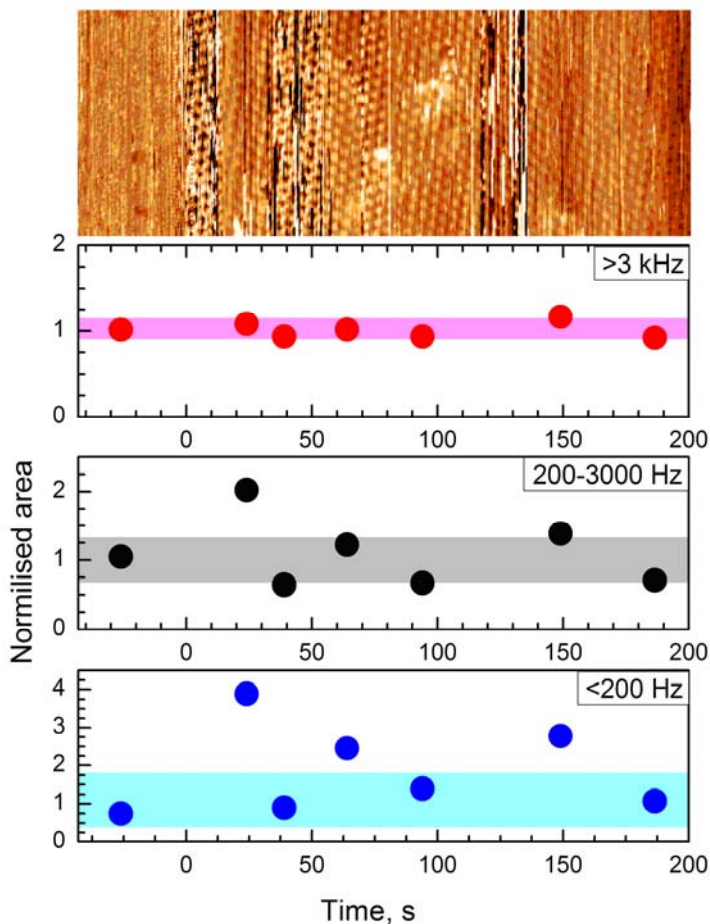


Figure 5.4 Topography of Pt(111) recorded ( $26 \times 10 \text{ nm}^2$ ,  $I=0.2 \text{ nA}$ ,  $V=0.3 \text{ V}$ ) while the surface is exposed to  $1 \times 10^{-4}$  mbar of oxygen. Circles show the noise level (normalized area) obtained for three frequency windows. Bars are marking the noise level regions for the bare surface in the same frequency windows.

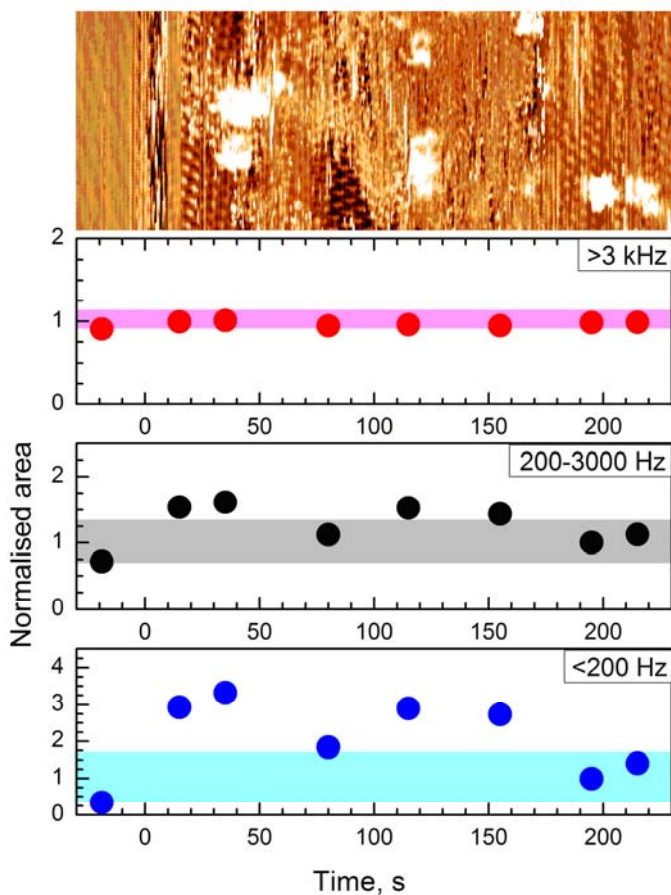


Figure 5.5 Topography of the Pt(111) recorded ( $26 \times 10 \text{ nm}^2$ ,  $I=0.2 \text{ nA}$ ,  $V=0.25 \text{ V}$ ) while the surface is exposed to  $1 \times 10^{-4} \text{ mbar}$  of the oxygen-carbon monoxide mixture ( $O_2:CO= 200:1$ ). Circles show the noise level (normalized area) obtained for three frequency windows. Bars are marking the noise level regions for the bare surface in the same frequency windows.

Gold is known to be inert for oxygen adsorption at room temperature and high vacuum [22]. We employ this property to verify if the interaction of oxygen with the STM tip influences the noise spectra. Figure 5.6 shows the noise intensity variation while scanning an Au(100) surface while  $1 \times 10^{-4}$  mbar of oxygen was introduced at some point. The range of noise intensity for the gold surface-W tip was determined for the bare surface in a number of separate experiments.

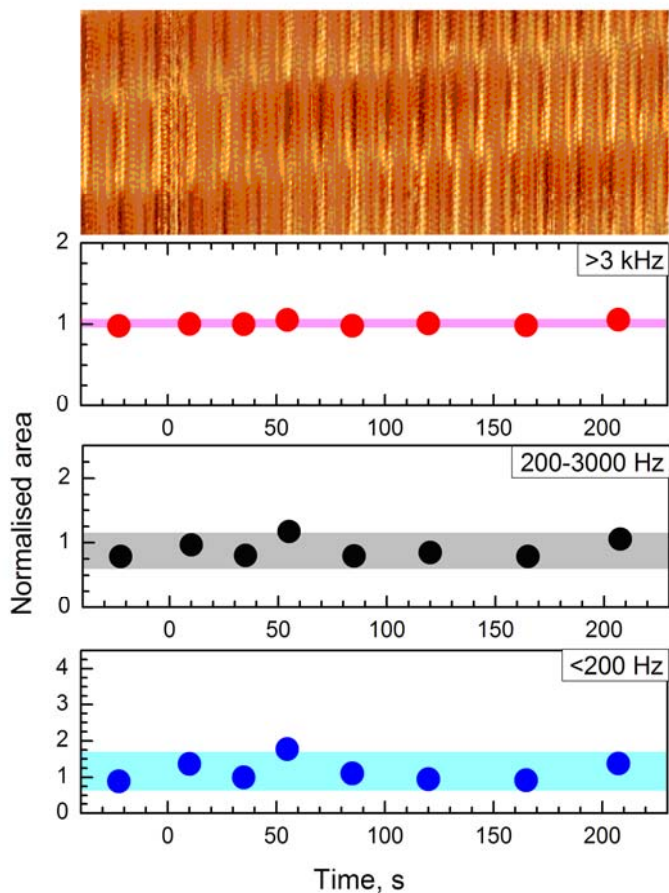


Figure 5.6 Topography of Au(100) recorded ( $26 \times 10 \text{ nm}^2$ ,  $I=0.2 \text{ nA}$ ,  $V=0.3 \text{ V}$ ) while the surface is exposed to  $1 \times 10^{-4}$  mbar of oxygen. Circles show the noise level (normalized area) obtained for three frequency windows. Bars are marking the noise level regions for the bare surface in the same frequency windows.

## 5.4 Discussion

The interpretation of the above results is complex as there are multiple sources contributing to the current transients of the tip-sample tunnel junction. It is important to separate the influence of interfering sources such as the noise of apparatus and tip instability to extract the noise caused by dynamical processes occurring on the surface.

None of the noise spectra measured while filling the chamber with carbon monoxide revealed noticeable changes in the noise level compared to the noise spectrum produced on the clean platinum surface (Figure 5.3). At the same time, corresponding STM images show that a stable layer of CO did not form immediately after the surface was exposed to CO. Thus, there was room for diffusion of the adsorbed carbon monoxide during the initial  $\sim 90$  seconds. This raises the question why the CO diffusion is not reflected as an increase in the STM noise. To answer this question, we first note that adsorption of CO induces changes in the LDOS such that the CO molecule is seen by STM as a protrusion of 10-40 pm depending on the adsorption site [21]. We also regularly observed surface corrugation of 10-20 pm for the ordered  $c(4 \times 2)$ -CO layer. Moreover, the noise level of our apparatus is low enough to obtain atomically resolved images of the clean Pt(111) surface with a corrugation of  $\approx 5$  pm (see for example Figure 2.4). Thus, we can exclude that a lack of spatial resolution in the  $z$  direction causes an apparent CO 'invisibility'. Therefore, we seek the answer in the temporal resolution of the apparatus. Extrapolating results of Wang et al. [12] to room temperature, one can obtain a hopping rate of  $\sim 100$  kHz for CO migration on Pt(111). This is at least one order of magnitude higher than the bandwidth of our I-V converter ( $< 10$  kHz). Carbon monoxide is simply too mobile on Pt(111) at 300K for its diffusion to be detected in our system.

A presence of oxygen in the reaction chamber triggered an increase in the tunnel current noise level (Figures 5.4 and 5.5). Both parts of the tunnel junction, i.e. the platinum substrate and the tungsten tip, may be responsible for this. The STM image in Figure 5.4 demonstrates that the platinum surface became covered by an  $O-p(2 \times 2)$  layer directly after oxygen was introduced at  $1 \times 10^{-4}$  mbar. Since the sticking probability of  $O_2$  for tungsten ( $s_0=0.5-1$  [23, 24]) is higher than for Pt(111) ( $s_0 \approx 0.06$ ), we may safely conclude that the tip was already oxidized when the noise spectra were recorded. The tungsten surface binds oxygen more strongly than platinum [15] and also hosts at least twice the amount of atomic oxygen compared to

Pt(111) [23, 24]. Therefore, we expect that fluctuations of the tunnel current are caused by the surface dynamics of oxygen on the substrate rather than processes affecting the tip. Indirect proof of this assertion is demonstrated for the gold surface, which is known to be inert towards O<sub>2</sub> adsorption [22]. The spectra measured on the Au(100) surface did not show an increase in the noise intensity after the chamber was filled with oxygen (Figure 5.6). However, there is no guarantee that the arrangement and nature of the tip apex was the same in the separate experiments in which measurements on the platinum and gold surfaces were done. The STM images in Figures 5.3 and 5.4 show a number of tip switching events during scanning. This indicates that changes in the LDOS of the tip apex may lead to the observed increases in noise spectra intensity.

## 5.5 Summary

A method using tunneling current transients to study catalytic reactions on metal surfaces was tested. Preliminary data obtained for CO oxidation gave inconclusive results regarding the applicability of this technique. The presence of CO did not affect the observed noise intensity. However, an increased intensity of current fluctuations was found when the platinum surface is exposed to oxygen and to the reactive mixture of oxygen and carbon monoxide. Although the tip instability can not be ruled out as a source of the detected current transients, the observed increase of the noise level is likely caused by the motion of the O<sub>ads</sub> species on the surface, suggesting that the low O mobility is the main source of the current fluctuations both during O adsorption and during the reaction of CO with adsorbed O.

## References:

- [1] M. Bowker and P. D. Davies, Scanning Tunneling Microscopy in Surface Science, Nanoscience and Catalysis, Wiley-VSH verlag GmbH & Co. KGaA, Weinheim, 2010.
- [2] G. Binnig, H. Fuchs, and E. Stoll, Surface Science 169 (1986) L295.
- [3] B. Koslowski, C. Baur, R. Moller, and K. Dransfeld, Surface Science 280 (1993) 106.
- [4] P. A. Sloan, Journal of Physics-Condensed Matter 22 (2010)
- [5] B. C. Stipe, M. A. Rezaei, and W. Ho, Physical Review Letters 81 (1998) 1263.
- [6] M. L. Lozano and M. C. Tringides, Europhysics Letters 30 (1995) 537.
- [7] J. Lagoute, T. Zambelli, S. Martin, and S. Gauthier, Image Analysis & Stereology 20 (2001) 175.
- [8] J. Wintterlin, J. Trost, S. Renisch, R. Schuster, T. Zambelli, and G. Ertl, Surface Science 394 (1997) 159.
- [9] M. O. Pedersen, L. Osterlund, J. J. Mortensen, M. Mavrikakis, L. B. Hansen, I. Stensgaard, E. Laegsgaard, J. K. Norskov, and F. Besenbacher, Physical Review Letters 84 (2000) 4898.
- [10] T. Tansel and O. M. Magnussen, Physical Review Letters 96 (2006)
- [11] K. Wang, C. Zhang, M. M. T. Loy, and X. Xiao, Physical Review Letters 94 (2005) 036103.
- [12] K. D. Wang, F. F. Ming, Q. Huang, X. Q. Zhang, and X. D. Xiao, Surface Science 604 (2010) 322.
- [13] M. Sumetskii, A. A. Kornyshev, and U. Stimming, Surface Science 307 (1994) 23.
- [14] J. V. Barth, H. Brune, B. Fischer, J. Weckesser, and K. Kern, Physical Review Letters 84 (2000) 1732.
- [15] J. V. Barth, Surface Science Reports 40 (2000) 75.
- [16] M. J. Rost, L. Crama, P. Schakel, E. van Tol, G. B. E. M. van Velzen-Williams, C. F. Overgaww, H. ter Horst, H. Dekker, B. Okhuijsen, M. Seynen, A. Vijftigschild, P. Han, A. J. Katan, K. Schoots, R. Schumm, W. van Loo, T. H. Oosterkamp, and J. W. M. Frenken, Review of Scientific Instruments 76 (2005) 053710.
- [17] F. Esch, C. Dri, A. Spessot, C. Africh, G. Cautero, D. Giuressi, R. Sergo, R. Tommasini, and G. Comelli, Review of Scientific Instruments 82 (2011) 053702.
- [18] J. Méndez, S. H. Kim, J. Cerdá, J. Wintterlin, and G. Ertl, Physical Review B 71 (2005) 085409.
- [19] F. Gao, S. M. McClure, Y. Cai, K. K. Gath, Y. Wang, M. S. Chen, Q. L. Guo, and D. W. Goodman, Surface Science 603 (2009) 65.



- [20] F. Biscarini, C. Bustamante, and V. M. Kenkre, *Physical Review B* 51 (1995) 11089.
- [21] M. L. Bocquet and P. Sautet, *Surface Science* 360 (1996) 128.
- [22] S. Carabineiro and B. Nieuwenhuys, *Gold Bulletin* 42 (2009) 288.
- [23] M. Bowker and D. A. King, *Surface Science* 94 (1980) 564.
- [24] T. Engel, H. Niehus, and E. Bauer, *Surface Science* 52 (1975) 237.
- [25] R. Möller, A. Esslinger, and K. Koslowski, *Appl. Phys. Lett* 55 (1989) 2360.



## Summary

The work presented in this thesis resulted from an NWO project on the use of current transient detection of surface-catalyzed chemical reactions by means of scanning tunneling microscopy. In line with the proposed idea, the oxidation of carbon monoxide was chosen as a probe reaction and the Pt(111) surface as the catalytically active substrate. An available Omicron VT-STM system was used as the central experimental setup. In order to test the proposal, a number of additional studies had to be performed. One of these was the preparation of tunnel probes (tips) that allowed for STM experiments with stable currents for long times, as described in Chapter 2. Initial performance studies led to modification of the UHV setup and additional detailed studies of CO oxidation were needed to gain the required level of control.

Temperature has an important effect on the dissociative adsorption of molecular oxygen on platinum surfaces and thereby on CO oxidation. In Chapter 3 it was shown that, if the substrate temperature is increased to 400-600 K, the total amount of oxygen adsorbed onto Pt(111) can be more than twice the well-established maximum coverage of 0.25 ML. While LEED and STM reveal a conventional  $p(2 \times 2)$  structure of the topmost layer, temperature programmed desorption measurements indicate that additional oxygen is stored under the surface of platinum. Reactivity measurements show that this sub-surface oxygen layer does not lower the activity of this platinum surface towards CO oxidation. Therefore, while a sub-surface oxygen layer does form under catalytically relevant temperatures on Pt(111), it has no great influence on the oxidizing ability of this surface. This sheds new light on the initial stages of platinum oxide formation and may help bridge the understanding of catalytic oxidation of CO on Pt in UHV and in high-pressure catalysis studies. The sub-surface oxygen is likely the precursor of the stoichiometric  $\alpha$ -PtO<sub>2</sub> formed in catalytic reactors and as such links catalytic oxidation reactions in UHV and at high pressure conditions.

An increase in substrate temperature brings an additional transition phenomenon into the studied system, as was also demonstrated in Chapter 3. It is the reversible migration of adsorbed oxygen into the substrate. From this, it was concluded that the reaction at room temperature would likely have the least possible sources of unwanted noise in the current transient experiments.

In Chapter 4, catalytic oxidation of carbon monoxide on Pt(111) surface was investigated by means of STM and LEED at room temperature and a total pressure of  $1 \times 10^{-4}$  mbar. In this regime  $O_2$  and CO compete for adsorption sites and, depending on the composition of the mixture, the platinum surface appears covered by a reactive ordered adlayer of atomic oxygen, by a reactive mixture of both adsorbates, or is blocked by a compact layer of adsorbed carbon monoxide. All three states were characterized and the transitions between them visualized with LEED and STM at the critical concentration of CO. In the intermediate state the platinum surface demonstrates a complex structure on the atomic scale with ordered islands of oxygen separated by regions without distinct order. While results fit well with titration studies and corresponding simulations, this “mixed” state is found to be not stable enough to sustain a continuous reaction under the conditions studied.

The analysis of current transients for a set of CO oxidation conditions that seemed appropriate from the previous studies, is presented in the last chapter of this thesis. We thus followed the original proposal for determining the noise level in the tunneling region and applied it to the  $Pt(111)+O_{2(gas \leftrightarrow adsorbant)}+CO_{(gas \leftrightarrow adsorbant)}$  system. The obtained results were inconclusive, as we expected the tunneling current noise to change as a result from changes in the adsorbent composition and its atomic geometry. In the experiment, an enhanced noise amplitude was observed only in the presence of oxygen. If the system artefacts could be put aside, one would be able to conclude that the reaction rate of carbon monoxide oxidation on Pt(111), or at least the STM noise associated with it, depends on oxygen surface diffusion.

## Samenvatting

Dit proefschrift beschrijft de resultaten van een door NWO gefinancierd project over de detectie en interpretatie van stroom transients, gemeten met een raster tunnel microscoop (“scanning tunneling microscope” STM), als gevolg van chemische reacties die plaats vinden aan metaal oppervlakken. De oxidatie van koolmonoxide (CO) aan een Pt(111) oppervlak werd daarbij gekozen als model reactie en bestudeerd met een Omicron VT-STM systeem. Alvorens de transients te meten, werd een aantal voorbereidende metingen gedaan. Eén daarvan was de preparatie van de dunne meetnaald (“tip”) waarmee gedurende lange tijd stabiele STM metingen gedaan kunnen worden, zoals beschreven in Hoofdstuk 2. De eerste metingen leiden vervolgens tot een aanpassing van het bijbehorende Ultra-Hoog Vacuum (UHV) apparaat en vervolgstudies aan de CO oxidatie waren nodig om de vereiste controle over de reactie te bewerkstelligen.

De temperatuur heeft een belangrijke invloed op de dissociatieve adsorptie van moleculair zuurstof en derhalve ook op de CO oxidatie. In Hoofdstuk 3 hebben we laten zien dat, als de temperatuur van het oppervlak naar 400-600 K wordt verhoogd, de totale hoeveelheid atomaire zuurstof dat aan het Pt(111) oppervlak adsorbeert, twee keer zo hoog kan zijn dan de algemeen aangenomen maximale bedekkingsgraad van 0.25. Hoewel LEED and STM een conventionele  $p(2 \times 2)$  structuur van de oppervlakte laag laten zien, geven temperatuur-geprogrammeerde desorptie metingen aan dat er extra zuurstof is opgeslagen onder het platina oppervlak. Reactiviteitsmetingen laten zien dat deze “sub-surface” zuurstoflaag de activiteit van het platina oppervlak voor de CO oxidatie niet verlaagt. Dat betekent dat hoewel er een sub-surface zuurstoflaag aan Pt(111) vormt onder katalytisch relevante condities, deze laag geen grote invloed heeft op de oxidatiecapaciteit van het oppervlak. Dit werpt een nieuw licht op de initiele stadia van de vorming van oppervlakte platina oxides en kan bijdragen aan het overbruggen van het begrip van de katalytische oxidatie van CO aan platina in UHV naar katalyse studies onder hoge druk.

Hoofdstuk 3 laat ook zien dat de verhoging van de temperatuur van het oppervlak leidt tot een extra overgangsfenomeen in het bestudeerde systeem, namelijk de reversibele migratie van geadsorbeerd zuurstof van het oppervlak naar de sub-oppervlakte lagen. Daaruit werd geconcludeerd dat de reactie bij kamertemperatuur vermoedelijk het minste last zou hebben van ongewenste ruis in de STM metingen.

In Hoofdstuk 4 werd de katalytische oxidatie van CO aan het Pt(111) oppervlak onderzocht met behulp van STM en LEED bij kamertemperatuur en een totale druk van  $1 \times 10^{-4}$  mbar. Onder deze omstandigheden gaan O<sub>2</sub> en CO een competitie aan voor adsorptie plaatsen en, afhankelijk van de samenstelling van het mengsel zal het platina oppervlak bedekt zijn door een reactieve geordende adlaag van atomair zuurstof, door een reactief mengsel van beide adsorbaten, of het is geblokkeerd door een compacte laag geadsorbeerd koolstof monoxide. Alle drie toestanden van het oppervlak en de overgangen tussen hen (bij een specifieke concentratie aan CO) konden worden gekarakteriseerd en gevisualiseerd met LEED and STM. In de intermediaire toestand vertoont het platina oppervlak een complexe structuur op atomaire schaal met geordende eilanden van zuurstof afgewisseld met gebieden zonder zichtbare orde. Hoewel de resultaten goed overeenkomen met titratie studies en bijpassende simulaties, is deze “mengtoestand” onder de gemeten omstandigheden niet stabiel genoeg om een continue reactie te onderhouden.

De analyse van de stroomtransients onder reactie omstandigheden zoals die zijn afgeleid uit de voorgaande hoofdstukken, zijn het onderwerp van het laatste hoofdstuk van het proefschrift. Hierbij volgden we het oorspronkelijke voorstel om de ruis in de STM tunneling stroom te meten voor het Pt(111)+O<sub>2(gas↔adsorbant)</sub>+CO<sub>(gas↔adsorbant)</sub> systeem. De verkregen resultaten waren niet eenduidig, aangezien we verwachtten dat de ruis het gevolg zou zijn van veranderingen in de lokale adsorbaat samenstelling en geometrie, aangezien dit een verandering zou moeten geven in de lokale elektronische toestandsdichtheid. In het experiment werd een verhoogde amplitude van de ruis alleen waargenomen in de aanwezigheid van zuurstof. Als we eventuele artefacten in het meetsysteem even buiten beschouwing laten, zou men kunnen concluderen dat de reactie snelheid voor CO oxidatie aan Pt(111), of op zijn minst de STM ruis die daar mee gepaard gaat, voornamelijk afhangt van de oppervlakte mobiliteit van zuurstof.



## Curriculum Vitae

Dima (Dmytro Leonidovich) Bashlakov was born in Ossora village (Kamchatka peninsula, USSR) on 4<sup>th</sup> of November 1980. He obtained his bachelor (2002) and master (2003) degrees in Kharkiv National University (Ukraine). Thereafter, he started his postgraduate education (2003-2006) in the B.Verkin Institute for Low Temperature Physics and Engineering of the National Academy of Science of Ukraine. At the conclusion of that study, Dima defended his thesis '*Point-contact spectroscopy of superconducting nickel borocarbide  $YNi_2B_2C$  and ferromagnetic-nonmagnetic metal heterocontacts*' in 2007. His diploma was approved on March 12, 2008 by the Presidium of the Higher Examination Board of Ukraine. In 2007, he was awarded the Prize for Young Scientists by the President of Ukraine and was admitted to the PhD program at Leiden University. He started his PhD research in March 2008 in the Catalysis and Surface Chemistry group with Prof. Dr. M. T. M. Koper as a promoter and Dr. A.I. Yanson as co-promoter. The results of his PhD research are presented in this thesis.